Potent and Selective Covalent Inhibition of the Papain-like Protease from SARS-CoV-2

Brian Sanders

Oak Ridge National Laboratory   https://orcid.org/0000-0001-9754-1687

Suman Pokhrel

Stanford University   https://orcid.org/0000-0003-2258-8768

Audrey Labbe

Oak Ridge National Laboratory

Irimpan Mathews

SLAC National Accelerator Laboratory

Connor Cooper

Oak Ridge National Laboratory

Russell Davidson

Oak Ridge National Laboratory

Gwyndalyn Phillips

Oak Ridge National Laboratory   https://orcid.org/0000-0001-5858-3825

Kevin Weiss

Oak Ridge National Laboratory   https://orcid.org/0000-0002-6486-8007

Qiu Zhang

Oak Ridge National Laboratory

Hugh O'Neill

Oak Ridge National Laboratory   https://orcid.org/0000-0003-2966-5527

Manat Kaur

Stanford University

Lori Ferrins

Northeastern University

Jurgen Schmidt

Los Alamos National Laboratory   https://orcid.org/0000-0002-8192-9940

Walter Reichard

University of Tennessee Health Science Center

Surekha Surendranathan

University of Tennessee Health Science Center

Jyothi Parvathareddy

University of Tennessee Health Science Center

Lexi Phillips

Utah State University

Christopher Rainville

Progenra Inc.

David Sterner

Progenra Inc.

Desigan Kumaran

Brookhaven National Laboratory

Babak Andi

Brookhaven National Laboratory   https://orcid.org/0000-0002-7666-639X

Gyorgy Babnigg

Argonne National Laboratory

Nigel Moriarty

Lawrence Berkeley National Laboratory   https://orcid.org/0000-0001-8857-9464

Paul Adams

Lawrence Berkeley Laboratory   https://orcid.org/0000-0001-9333-8219

Andrzej Joachimiak

University of Chicago   https://orcid.org/0000-0003-2535-6209

Brett Hurst

Institute for Antiviral Research, Utah State University   https://orcid.org/0000-0003-1025-5878

Suresh Kumar

Progenra   https://orcid.org/0000-0002-1940-772X

Tauseef Butt

Progenra

Colleen Jonsson

University of Tennessee Health Science Center

Soichi Wakatsuki

Stanford University   https://orcid.org/0000-0001-5896-7968

Stephanie Galanie

Oak Ridge National Lab

Martha Head

Oak Ridge National Laboratory

Jerry Parks (✉ parksjm@ornl.gov)

Oak Ridge National Laboratory   https://orcid.org/0000-0002-3103-9333

Article

Keywords:

Abstract

Direct-acting antivirals are needed to combat coronavirus disease 2019 (COVID-19), which is caused by severe acute respiratory syndrome-coronavirus-2 (SARS-CoV-2). The papain-like protease (PLpro) domain of Nsp3 from SARS-CoV-2 is essential for viral replication. In addition, PLpro dysregulates the host immune response by cleaving ubiquitin and interferon-stimulated gene 15 protein (ISG15) from host proteins. As a result, PLpro is a promising target for inhibition by small-molecule therapeutics. Here we have designed a series of covalent inhibitors by introducing a peptidomimetic linker and reactive electrophile onto analogs of the noncovalent PLpro inhibitor GRL0617. The most potent compound inhibited PLpro with $k_{inact}/K_I = 10,000$ M^{-1} s^{-1}, achieved sub-µM EC$_{50}$ values against three SARS-CoV-2 variants in mammalian cell lines, and did not inhibit a panel of human deubiquitinases at > 30 µM concentrations of inhibitor. An X-ray co-crystal structure of the compound bound to PLpro validated our design strategy and established the molecular basis for covalent inhibition and selectivity against structurally similar human DUBs. These findings present an opportunity for further development of covalent PLpro inhibitors.

Introduction

COVID-19 emerged globally with the rapid spread of the previously unrecognized beta-coronavirus SARS-CoV-2.[1, 2] The virus is highly transmissible and can lead to severe, and in many cases life-threatening, respiratory disease. Few effective drugs have been developed to date, with molnupiravir[3] and nirmatrelvir[4] being the only currently available oral antivirals for treating SARS-CoV-2 infections. Although vaccines and therapeutic antibodies are effective in preventing COVID-19 or reducing its severity, respectively, the emergence of some variants of concern (i.e., Omicron) limits their effectiveness. Thus, there is an urgent need to develop antiviral therapeutics that are effective against SARS-CoV-2 and related coronaviruses.

The SARS-CoV-2 genome encodes two cysteine proteases, the 3-chymotrypsin-like protease (3CLPro or Mpro) and the papain-like protease (PLpro), both of which are essential for viral maturation. PLpro is a 35-kDa domain of Nsp3, a 215-kDa multidomain protein that is key to maturation of the viral replicase-transcriptase complex (RTC).[5] PLpro cleaves the viral polyproteins pp1a and pp1ab at three sites to produce nonstructural proteins Nsp1, Nsp2, and Nsp3. In addition to RTC maturation, PLpro enables evasion of the host immune response by cleaving ubiquitin and the ubiquitin-like protein ISG15 from host protein conjugates.[6−8] Compared to PLpro from SARS-CoV (SARS-CoV PLpro), SARS-CoV-2 PLpro displays decreased deubiquitinase activity and enhanced deISGylation activity.[9−11] In addition, PLpro attenuates type I interferon pathways involved in mediating antiviral immune responses.[10] Inhibition of SARS-CoV-2 PLpro was shown to reduce viral replication in Vero CCL-81 cells[12] and to maintain the host interferon pathway.[10]

PLpro consists of thumb, fingers, and palm subdomains common to other ubiquitin-specific proteases, and an N-terminal ubiquitin-like domain involved in substrate recognition (Fig. 1a). The active site, which is located at the interface of the thumb and palm subdomains, consists of a catalytic triad comprising Cys111, His272, and Asp286.[12–14] Besides the catalytic Cys111, four Cys residues coordinate a structural Zn^{2+} cation in the fingers subdomain and six additional Cys residues are present elsewhere in the protein. Of all the cysteines in PLpro, Cys111 is the most prone to oxidation,[14] indicating that it is unique in its reactivity toward electrophiles.

Protein substrates of PLpro consist of a Leu-X-Gly-Gly peptide motif (X = Arg, Lys, or Asn), with proteolytic cleavage occurring after the second Gly residue.[6] Leu and X occupy the S4 and S3 subsites, respectively, and the two Gly residues occupy the S2 and S1 subsites, which are covered by a β-hairpin "blocking loop" (BL2 loop) that forms a narrow groove leading to the active site (Fig. 1).[12] As a result, only extended peptide substrates with two Gly residues at the P1 and P2 positions can be accommodated in this space.[11, 12]

Several noncovalent inhibitors of PLpro have been developed that competitively inhibit PLpro.[14–17] The naphthylmethylamine compound GRL0617 inhibits SARS-CoV PLpro with an IC_{50} of ~ 0.6 μM and inhibits viral replication in Vero E6 cells with EC_{50} = 14.5 μM.[15] The desamino analog of GRL0617 exhibits similar inhibitory activity (IC_{50} = 2.3 μM; EC_{50} = 10 μM), as does the N-acetylated analog (IC_{50} = 2.6 μM; EC_{50} = 13.1 μM). GRL0617 exhibits similar inhibition activity against SARS-CoV-2 PLpro.[10, 14, 18] Importantly, GRL0617 does not inhibit the structurally similar human deubiquitinases (DUBs). The IC_{50} values for GRL0617 toward HAUSP, the deISGylase USP18, and the ubiquitin C-terminal hydrolases UCH-L1 and UCH-L3 are all > 100 μM.[15] In addition, GRL0617 does not display cytotoxicity at concentrations up to 50 μM in cell viability assays. Crystallographic studies[14, 15] have revealed key interactions between PLpro and GRL0617 including (i) a hydrogen bond between the backbone N-H of Gln269 and the amide carbonyl of the inhibitor, (ii) a hydrogen bond between the N-H of the GRL0617 amide and the carboxylate side chain of Asp164, and (iii) an edge-to-face interaction of the naphthyl group of GRL0617 and Tyr268 (Fig. 1b).

Naphthylmethylamine-based[19] noncovalent PLpro inhibitors provide a valuable starting point for further optimization. Here we have designed covalent inhibitors of PLpro based on GRL0617. We report in vitro inhibition (IC_{50}, k_{inact}/K_I), cytopathic protection (EC_{50}, EC_{90}) and cytotoxicity (CC_{50}), electrospray ionization mass spectrometry, X-ray crystallography, enzyme selectivity, metabolic stability, and pharmacokinetics data. We show that the most promising candidate is a highly potent and selective covalent inhibitor of PLpro from SARS-CoV-2.

Results And Discussion

We designed a series of covalent PLpro inhibitors based on the noncovalent inhibitor GRL0617 (**Figures 2 and 3**). Previous crystallographic studies have revealed that the phenylmethyl group of GRL0617 points

toward the active site but is located >7 Å from Sg of Cys111 (**Figure 1b**).[14] We reasoned that replacing the methyl substituent of GRL0617 with a hydrolytically stable linker connected to an electrophile capable of reacting with Cys111 would yield a potent covalent inhibitor of PLpro. We chose an *N, N'*-acetylacetohydrazine linker as a linear Gly-Gly peptidomimetic that could reach through the narrow S2 and S1 groove to the active site while also preserving some of the hydrogen-bonding interactions (e.g., with Gly163 and Gly271) afforded by natural peptide substrates. To the resulting linker we appended a series of electrophiles including a fumarate methyl ester,[20] chloroacetamide,[21] propiolamide, cyanoacetamide, and α-cyanoacrylamide.

To help prioritize designed molecules for synthesis and testing, we performed covalent docking of each candidate molecule to PLpro (**Figure 2**). We also docked each molecule non-covalently to assess the favorability of pre-covalent binding. We used an ensemble of 50 structural models derived from X-ray crystallographic data to account for protein flexibility[14] and included selected crystallographic waters during docking, including those that are known to remain stably bound in the S4 subsite in the presence of noncovalent inhibitors (**Figure S1**).[14, 15] All candidate inhibitors contained the naphthylmethylamine core of GRL0617 and we aimed for our modified compounds to recapitulate its crystallographic binding mode. To assess pose similarity, we measured the maximum common substructure RMSD (MCS-RMSD) between the docked poses of the candidate inhibitors and the crystallographic pose of GRL0617. In general, the core of the inhibitor designs and their noncovalent precursors reproduced the binding mode of GRL0617 to within 2 Å RMSD, maintaining interactions with Asp164, Tyr268, and Gln269 while the linker simultaneously occupied the S2 and S1 subsites to place the electrophilic group near the catalytic Cys111 nucleophile (**Figure 2** and **Figure S2**). Compounds were prioritized for synthesis based on low MCS-RMSD values (≤ 2 Å), favorable noncovalent and covalent docking scores (**Figure S3** and **Supplementary Data File 1**), and synthetic tractability.

We synthesized compounds **2-15** through a straightforward approach beginning from an amide coupling of (*R*)-(+)-1-(1-napthyl)ethylamine and 2-(3-methoxy-3-oxopropyl)benzoic acid derivatives, where R_1 = H or NHAc (**Figure 3**). Following this coupling, we reacted the ester in **3** and **4** with $N_2H_4 \cdot H_2O$ in refluxing EtOH to afford the hydrazide group in **5** and **6** in near quantitative yield. With the respective hydrazides in hand, we installed a variety of electrophiles using acid chlorides. Notably, the solubility of **5** and **6** were dramatically different from each other and required separate conditions for installation of the electrophilic groups. DIPEA/DCM was used for **5** (R_1 = H) and K_2CO_3/DMF was used for **6** (R_1 = NHAc). Overall, we synthesized seven potential covalent inhibitors (**7-13**) and two additional noncovalent GRL0617 derivatives, namely compounds **14** (R_1 = H) and **15** (R_1 = NHAc).

The synthesized compounds were then assessed for potential anti-SARS-CoV-2 activity in a biochemical assay using purified PLpro and a ubiquitin C-terminus-derived fluorogenic substrate Z-RLRGG-AMC[15, 22, 23] (**Figure 3** and **Figure S4**). IC_{50} values were determined following a 30-minute incubation of PLpro with inhibitor (**Figure S5**). Of the noncovalent analogs of GRL0617, we found that both **14** and **15** had increased IC_{50} values, with the *N*-acetylated compound **15** having an IC_{50} more like that of GRL0617

(**Table 1**). Encouragingly, extending the tolyl methyl to include a substantially larger peptidomimetic group maintained potency. For example, addition of the linker alone without an electrophile to form **5** led to an IC_{50} of 24 mM (**Figure 3** and **Figure S5**). The introduction of five different electrophilic groups to produce compounds **7**, **9**, and **11-13** resulted in improved IC_{50} values for all except α-cyanoacrylamide **13**. Time-dependent inhibition assays were performed because time-dependence is consistent with multiple mechanisms of slow-binding inhibition, including covalent inhibition via bond formation between Cys111 and the electrophile. Installation of a chloroacetamide electrophile to form **9** improved the IC_{50} compared to **5** to 5.4 mM after 30-min incubation and resulted in a k_{inact}/K_I of 100 M^{-1} s^{-1} (**Figure S6**), where k_{inact}/K_I is a second-order rate constant describing the efficiency of the overall conversion of free enzyme to the covalent enzyme-inhibitor complex.[24] Similarly, the IC_{50} and k_{inact}/K_I for *N*-acetylated analog **10** are 4.4 mM and 120 M^{-1} s^{-1}, respectively.

Based on previous success in incorporating a vinyl methyl ester electrophile into tetrapeptide-based, irreversible covalent inhibitors of PLpro,[11] we reasoned that incorporating a similar ester into our covalent inhibitor candidates would occupy the oxyanion hole in the active site and that the ester carbonyl oxygen would engage in a hydrogen bond with the indole N-H of Trp106. Fumarate methyl ester **7** had an IC_{50} of 94 nM after 30-minute incubation and k_{inact}/K_I = 10,000 M^{-1} s^{-1}, indicating potent inhibition (**Table 1** and **Figure S6**). *N*-acetylated analog **8** showed similar potency, with IC_{50} and k_{inact}/K_I = 230 nM and 14,000 M^{-1} s^{-1}, respectively. To examine the inhibitory activity of other electrophiles, we synthesized and performed time-independent inhibition assays with cyanoacetamide **11** (IC_{50}, 8 mM), propiolamide **12** (98 nM), and a-cyanoacrylamide **13** (>200 mM). Time-dependent inhibition was observed for **12**, but not for **11** or **13** (**Figure S7**). To provide additional evidence for a covalent mechanism of action, compounds **7-10** and **12** were incubated with PLpro, and the protein intact masses were determined by electrospray ionization mass spectrometry (ESI-MS). Covalent adduct formation with PLpro was confirmed for these five compounds (**Figure 4c**, **Figure S8**, and **Table S1**).

Table 1. PLpro inhibition and SARS-CoV-2 antiviral activity.

Compound	R_1[a]	Electrophile	IC_{50} (mM)[b]	Time dep.	k_{inact}/K_I (M^{-1} s^{-1})	EC_{50} (mM)[c]	Cytotox. (<30 mM)
GRL0617	NH_2	NA	1.2	no	NA	ND	ND
3	H	NA	>100	no	NA	ND	ND
5	H	NA	24	no	NA	ND	ND
7	H	fumarate ester	0.094	yes	10,000	1.1 (0.123)[d]	no
8	NHAc	fumarate ester	0.230	yes	14,000	no CPE	no
9	H	chloroacetamide	5.4	yes	103	34	no
10	NHAc	chloroacetamide	4.4	yes	120	no CPE	no
11	H	cyanoacetamide	8.0	no	ND	no CPE	no
12	H	propiolamide	0.098	yes	4,800	no CPE	yes
13	H	α-cyanoacrylamide	>200	no	ND	no CPE	yes
14	H	NA	100	ND	NA	no CPE	no
15	NHAc	NA	6.2	ND	NA	no CPE	no

[a] Structures are shown in Figure 3.

[a] Measurement after 30-minute incubation.

[b] Cytopathic effect in SARS-CoV-2-infected Vero E6 cells. EC_{50} for remdesivir = 0.74 mM.

[c] Value in parentheses obtained in the presence of the efflux inhibitor CP-100356.

NA = not applicable; ND = not determined.

We next assessed the ability of selected inhibitors to protect Vero E6 cells from virus-induced cell death, represented by EC_{50} (**Figure 4d** and **Figure S9**), by incubating cells with and without compound and then infecting them with SARS-CoV-2.[25] Uninfected cells were used to assess the cytotoxicity of the compounds, represented by CC_{50} (**Figure 3**). Compound **7** displayed notable antiviral activity with an EC_{50} of 1.1 μM, comparable to that of the remdesivir positive control (0.74 μM). Chloroacetamide **9** also displayed antiviral activity, although with less potency (34 mM). Neither **7** nor **9** displayed evidence of cytotoxicity (CC_{50} > 30 mM). Compounds **8** and **10**, which have *N*-acetylated phenyl substituents, showed insignificant cytoprotective effects. Both **12** and **13** were cytotoxic with CC_{50} values of 1-5 μM, suggesting that propiolamide and α-cyanoacrylamide electrophiles were too reactive, lack specificity, or both.

In addition to its role in processing the replicase polyprotein, SARS-CoV-2 PLpro displays deubiquitinase and de-ISG15ylase activity.[12, 26] To ensure that the most promising covalent inhibitors, **7** and **9**, can inhibit these physiologically relevant activities, IC_{50} values were obtained with Ub-rhodamine and ISG15-CHOP2 substrates (**Table S2**). Compound **7** inhibited PLpro with Ub-rhodamine and ISG15 substrates with IC_{50} values of 76 and 39 nM, respectively. The corresponding IC_{50} values for **9** with these two substrates were 1.96 μM and 20.2 μM, respectively.

Although small molecule-mediated inhibition has been reported for recombinant PLpro domain and for truncated Nsp3,[27] direct inhibition of full-length Nsp3 has not yet been demonstrated. Thus, we expressed

full-length hemagglutinin (HA)-Nsp3 in HEK293T cells and purified the enzyme using anti-HA immunoprecipitation (**Figure 5**). We found that compound **7** potently inhibited the deISGylase activity of full-length Nsp3 (IC_{50} = 0.038 mM). In contrast, GRL0617 showed much weaker inhibition (IC_{50} = 7.3 mM) under the same assay conditions.

To assess the efficacy of **7** against various SARS-CoV-2 strains, we performed CPE assays with Vero E6 cells infected with the USA-WA1/2020, Delta (B.1.617.2), or Omicron (B.1.1.529) variant (**Table 2**). Vero cells overexpress the efflux transporter P-glycoprotein (P-gp, also called MDR1 or ABCB1), so we performed assays of **7** in the presence of the P-gp inhibitor CP-100356.[28] Using a neutral red staining assay, we observed variant-dependent EC_{50} values of 0.068 mM for USA-WA1/2020, 0.29 mM for Delta, and 0.68 mM for Omicron. The origin of these differences is unclear, but we note that there are no characteristic mutations in the PLpro region of Nsp3 from the B.1.617.2 or B.1.1.529 variants relative to USA-WA1/2020.

Table 2. Cytopathic effect of compound 7 against three variants of SARS-CoV-2 in Vero E6 cells in the presence of 2 mM CP-100356. The RNA-dependent RNA polymerase inhibitor EIDD-1931 was used as a positive control.

Strain	Compound	EC_{50}[a] (mM)	CC_{50}[b] (mM)	SI_{50}[c]
USA-WA1/2020	7	0.068	>10	>150
	EIDD-1931	0.3	>100	>330
Delta (B1.617.2)	7	0.29	>10	>34
	EIDD-1931	0.31	>100	>320
Omicron (B1.1.529)	7	0.68	>10	>34
	EIDD-1931	0.3	>100	>330

[a] EC_{50} = 50% effective concentration

[b] CC_{50} = 50% cytotoxic concentration

[c] SI_{50} = CC_{50}/EC_{50}

To provide further confirmation of the antiviral activity of compounds in human cells, we evaluated the compounds in virus yield reduction assays using Caco-2 cells. We measured EC_{90} values for **7** in Caco-2 cells infected with the USA-WA1/2020, Delta (B.1.617.2), or Omicron (B.1.1.529) variant (**Table 3**). In contrast to the cytopathic protection assays performed with Vero 76 cells, the results varied more substantially among strains in this case. The EC_{90} was 0.26 μM for USA-WA1/2020, >10 μM for Delta, and 2.4 μM for Omicron. The reason for the weaker activity against the Delta and Omicron variants is unclear.

Table 3. Cytopathic Effect Assay Data for Compound 7 Against Three Variants of SARS-CoV-2 in Caco-2 Cells. The RNA-dependent RNA polymerase inhibitor EIDD-1931 was used as a positive control.

Strain	Compound	$EC_{90}{}^a$ (mM)	$CC_{50}{}^b$ (mM)	$SI_{90}{}^c$
USA-WA1/2020	7	0.26	>10	>38
	EIDD-1931	0.12	94	780
Delta (B1.617.2)	7	>10	>10	0
	EIDD-1931	4.9	>100	>20
Omicron (B1.1.529)	7	2.4	>10	>4.2
	EIDD-1931	2.9	>100	>34

^{a} EC_{90} = 90% effective concentration

^{b} CC_{50} = 50% cytotoxic concentration

^{c} SI_{90} = CC_{50}/EC_{90}

Following the promising results from *in vitro* assays and mass spectrometry experiments, we determined a crystal structure of wild-type PLpro in complex with **7** at 3.10 Å resolution (**Table S3**). The electron density maps show clear densities for PLpro, Zn cations, and **7**, confirming the design concept of this compound and revealing key interactions with PLpro (**Figure 6**). A covalent bond is present between Sg of Cys111 and the b carbon of the ester of **7** (**Figure 6a**). The carbonyl oxygen of the ester accepts hydrogen bonds from the indole side chain of Trp106, like that of the tetrapeptide-based covalent inhibitor VIR251,[11] and from the side chain of Asn109. The *N,N'*-acetylacetohydrazine moiety was designed to link the electrophile and the naphthylmethylamine core while also hydrogen bonding with residues in the S1-S2 groove. Indeed, the crystal structure revealed that the proximal and distal carbonyl oxygens of the linker interact with the backbone N-H groups of Gly163 and Gly271, and the proximal and distal N-H groups of this moiety participate in hydrogen bonds with the carbonyl backbones of Gly271 and Gly163. As intended, the carbonyl oxygen and N-H group of the amide adjacent to the naphthyl group of **7** are hydrogen bonded with the N-H backbone of Gln269 and the carboxylate side chain of Asp164. Compound **7** makes five main-chain and three side-chain hydrogen bonding interactions in the binding site. In addition, the side chains of Tyr268 and Gln269 interact with **7** similarly to GRL0617. Electron density for the methyl group of the ester of **7** was not visible. It is possible that the ester linkage is flexible and adopts multiple conformations or that it could have been hydrolyzed after covalent bond formation. Encouragingly, the covalently docked pose for **7** agrees closely with the co-crystal structure (**Figure 6b**).

We determined the metabolic stability of selected compounds in human, rat, and mouse liver microsomes and the corresponding S9 fractions (**Tables S4** and **S5**). Chloroacetamide **9** demonstrated very short half-lives of 7 and 3 minutes in human liver microsomes and S9 fractions, respectively, likely due to the highly reactive electrophile. Non-covalent inhibitor **14** exhibited a half-life of 41 min in human liver microsomes and >60 min in the S9 fraction and conversion of **14** to its covalent counterpart **7** maintained the half-life (50 min in microsomes and 60 min in S9). Analysis of **14** and **7** with MetaSite 6.0.1[32] suggested that

successive oxidations of the tolyl methyl of **14** are the predominant metabolic liability, followed by the benzylic methylene (**Figure S11**). Given that the linker and electrophile replaced the labile methyl group, it is unsurprising that the benzylic methylene is predicted to be the primary site of metabolism for **7**. To address the benzylic liability several modifications could be pursued, including substitution of the benzylic position with heavy atoms such as fluorine[33] or deuterium[34] to increase steric hindrance,[35] or blocking the site of metabolism via replacement of the tolyl methyl with cyclopropyl.[36] A recent report of non-covalent PLpro inhibitors showed that replacing the naphthyl group in GRL0617 with substituted 2-phenylthiophenes yielded inhibitors that mimic the binding interaction of ubiquitin with Glu167 of PLpro, simultaneously improving IC_{50} values and metabolic stability.[37] Thus, replacing the naphthyl group with substituted 2-phenylthiophenes[37] is also expected to be beneficial.

We advanced **7** into a pharmacokinetic study to assess its *in vivo* exposure. Male ICR mice were dosed with 10 mg/kg (PO) or 3 mg/kg (IV) to obtain a complete picture of the PK/PD profile. Unfortunately, **7** was not orally bioavailable and there was no exposure recorded following PO dosing. The PK parameters following IV dosing are summarized in **Table S6.** Little exposure was observed and the levels of **7** did not meet the threshold for progression into an in vivo efficacy study.

Numerous research efforts have focused on developing inhibitors of 3CLpro, but relatively few have focused on PLpro inhibition.[38, 39] A predominant reason for the emphasis on 3CLpro as an antiviral target is that there are no structural homologs in the human proteome, whereas PLpro bears structural similarity to human DUBs and deISGylases. However, our findings demonstrate that covalent inhibition of PLpro is a promising strategy for developing potent and selective therapeutics to combat SARS-CoV-2. Furthermore, a crystal structure of our most promising inhibitor covalently bound to PLpro provides insight that will facilitate the development of next-generation PLpro inhibitors with enhanced pharmacokinetic and pharmacodynamic properties.

Declarations

ACKNOWLEDGMENTS

AUTHOR CONTRIBUTIONS

B.C.S., S.G., S.W., M.S.H., and J.M.P. conceived the study.

B.C.S., S.G., and J.M.P. designed the candidate covalent inhibitors.

N.W.M. and P.D.A. generated the crystallographic ensemble.

R.B.D., C.J.C., and J.M.P. performed the docking and analysis.

B.C.S. and J.G.S. performed the chemical syntheses.

G.P., K.L.W., S.P., Q.Z., D.K., and H.O. expressed and purified the protein.

A.L. performed and analyzed in vitro enzyme inhibition assays.

S.G. supervised enzyme inhibition assays and performed and analyzed intact protein mass spectrometry experiments.

S.P., I.I.M., B.A., and G.B. crystallized the protein.

S.P. and I.I.M. solved the X-ray structures.

M.K. and S.W. performed the deubiquitinase structural analysis.

W.R. and S.S. performed and analyzed BSL3 cell-based antiviral assays.

C.R. performed cellular and biochemical experiments on Nsp3.

D.E.S. generated plasmids containing SARS-CoV-2 HA-Nsp3 used for mammalian expression.

S.K. designed Nsp3 experiments and analyzed data.

C.B.J. designed and supervised BSL3 antiviral assays and performed data analyses.

L.P. Conducted BSL3 antiviral assays in Caco-2 and Vero E6 cells

B.L.H. designed and supervised BSL3 antiviral assays and performed data analysis.

L.F., B.C.S., M.S.H., and J.M.P. analyzed the metabolic stability data.

T.R.B. and M.S.H. provided program oversight and analyzed data.

B.C.S., S.P., I.I.M., C.J.C., S.K., C.B.J., S.G., S.W., and J.M.P. wrote the paper.

COMPETING INTERESTS

B.C.S., S.G., and J.M.P. are inventors on a patent application on covalent PLpro inhibitors.

ORCID

Brian C. Sanders 0000-0001-9754-1687

Audrey Labbé 0000-0002-9802-665X

Suman Pokhrel 0000-0003-2258-8768

Irimpan Mathews 0000-0001-6254-3519

Connor J. Cooper 0000-0002-5527-9948

Russell B. Davidson 0000-0003-2364-4039

Gwyndalyn Phillips 0000-0001-5858-3825

Kevin L. Weiss 0000-0002-6486-8007

Qiu Zhang 0000-0002-5506-4955

Hugh O'Neill 0000-0003-2966-5527

Lori Ferrins 0000-0001-8992-0919

Jurgen G. Schmidt 0000-0002-8192-9940

Desigan Kumaran 0000-0002-6121-5350

Babak Andi 0000-0002-7666-639X

Gyorgy Babnigg 0000-0002-9838-1803

Nigel W. Moriarty 0000-0001-8857-9464

Paul D. Adams 0000-0001-9333-8219

Andrzej Joachimiak 0000-0003-2535-6209

Brett L. Hurst 0000-0003-1025-5878

Colleen B. Jonsson 0000-0002-2640-7672

Soichi Wakatsuki 0000-0001-5896-7968

Stephanie Galanie 0000-0001-5712-2568

Martha S. Head 0000-0001-7452-4753

Jerry M. Parks 0000-0002-3103-9333

Methods

Docking preparation. The 2.09 Å X-ray co-crystal structure of the C111S mutant of PLpro with GRL0617 (PDB entry 7JIR)[14] was used for the docking calculations. Rather than docking to a single structure, we used Phenix[40] to generate an ensemble[41] of 50 conformations from the corresponding crystallographic data in which conformations were sampled to generate an ensemble that collectively fit the data better than any single model. This approach provides valuable information about regions of high and low conformational variability in the protein, such as the BL2 loop, which is known to undergo large conformational changes upon substrate or inhibitor binding. Ser111 was converted back to Cys in all models.

Selected water molecules present in the models were retained during docking. Cys111 was modeled as a neutral thiol and His272 was protonated on Nε in accordance with its local hydrogen bonding environment and the proton transfer chemistry that is expected to occur during catalysis. Other histidines were protonated based on their inferred hydrogen bonding patterns. All other residues were protonated according to their canonical pH 7.0 protonation states. The program *tleap* from AmberTools20[42] was used to prepare the parameter and coordinate files for each structure. The ff14SB force field[43] and TIP3P water model[44] were used to describe the protein and solvent, respectively. Energy minimization was performed using *sander* from AmberTools20 with 500 steps of steepest descent, followed by 2000 steps

of conjugate gradient minimization. Harmonic restraints with force constants of 200 kcal mol^{-1} Å^{-1} were applied to all heavy atoms during energy minimization.

The peptide substrate binding cleft of PLpro spans ~30 Å along the interface of the palm and thumb domains (**Figure S1**). Thus, we defined a rectangular docking box spanning the entire binding cleft (S1-S4 sites) and the active site (catalytic triad). AutoGrid Flexible Receptor (AGFR)[45] was used to generate the receptor files for both noncovalent and covalent docking using a grid spacing of 0.25 Å. All docking calculations were performed with AutoDock Flexible Receptor (ADFR).[45] Compounds with electrophilic groups were docked both noncovalently (i.e., in the reactive form with an explicit electrophile present) and covalently (i.e., in the post-reactive Cys111 adduct form).

Ligand preparation. SMILES strings for candidate inhibitor designs were converted to PDB format using Open Babel[46] and Python/RDKit[47] scripts. Covalent docking with AutoDockFR requires that ligands be modified such that they include the covalent linkage to the side chain of the reactive residue, in this case Cys111, which then serves as an anchor to place the ligand approximately in the binding site.[45] Thus, the Ca and Cb atoms of Cys111 were used as anchors and the backbone N atom of Cys111 was used to define a torsional angle connecting the covalently bound ligand and the protein. MGLTools 1.5.6[48] was used to generate PDBQT files for ligands and receptors. Only polar hydrogens were retained during docking.

All candidate inhibitors considered in this work include the naphthylmethylamine core of GRL0617, for which co-crystal structures are available.[14] We expected that our covalent compounds would adopt a pose like GRL0617. Thus, to assess the similarity between the poses of docked candidate ligands and GRL0617 in the X-ray structure, we calculated the maximum common substructure (MCS) RMSD between them. MCS-RMSDs were calculated for all poses with docking energies within 3 kcal/mol of the overall most favorable pose for each candidate inhibitor. Compounds were prioritized for synthesis that had docked poses with MCS-RMSD values ≤2 Å and favorable noncovalent and covalent docking scores (**Figure S2** and **Supplementary Data File 1**). Figures were generated with PyMOL.[49]

Synthesis and Characterization of Compounds. All reagents were purchased from commercial suppliers and used as received unless otherwise noted. Anhydrous acetonitrile (MeCN), dichloromethane (CH$_2$Cl$_2$), ethanol (EtOH), dimethylformamide (DMF), tetrahydrofuran (THF), methanol (MeOH), and diethyl ether (Et$_2$O) were purchased from commercial sources and maintained under dry N$_2$ conditions. Amide couplings and reactions with acid chlorides were performed under N$_2$ using standard Schlenk-line techniques. Compound **1** was purchased from commercial sources and used as received. ^{1}H and ^{13}C NMR spectra were recorded in the listed deuterated solvent with a Bruker Avance III HD 500 MHz NMR spectrometer at 298 K with chemical shifts referenced to the residual protio signal of the deuterated solvent as previously reported.[50] Low-resolution mass data were collected on an Agilent 6470AA Triple Quadrupole LC/MS system. High-resolution mass data were collected on a Waters Synapt HDMS QTOF mass spectrometer. Following the initial synthesis and screening of compounds **2-15**, compound **7** was

produced on the gram-scale following the same procedures described below. Purity was analyzed by analytical HPLC and Thermo LTQ MS with electrospray ionization in the positive mode with a Waters BEH 130, 5 µm, 4.6 × 150 mm C18 column, linear gradient from 90:10 to 0:100 water/acetonitrile in 10 min at a flow rate of 1 mL/min. (**Supplementary Data File 2**).

5-acetamido-2-(3-methoxy-3-oxopropyl)benzoic acid (2). To a 15 mL solution of DCM was added 0.300 g (1.344 mmol) of 5-amino-2-(3-methoxy-3-oxopropyl)benzoic acid and cooled to 0 ºC. Acetic anhydride (1.3 mL, ~13 mmol) was added slowly while stirring. The solution was allowed to reach RT overnight, followed by addition of saturated NH_4Cl and extraction with DCM (3 × 50 mL). The organic phases were combined and dried with $MgSO_4$ and concentrated under reduced pressure to afford a pale-yellow syrup (0.195 g, 0.735 mmol, 55%). ^1H NMR (500 MHz, DMSO-d_6, δ from residual protio solvent) δ 12.40 (s, br, 1H), 10.00 (s, 1H), 8.03 (s, 1H), 7.67 (d, J = 8.3 Hz, 1H), 7.23 (d, J = 8.3 Hz, 1H), 3.57 (s, 3H), 3.10 (t, J = 7.7 Hz, 2H), 2.56 (t, J = 7.7 Hz, 2H), 2.03 (s, 3H). ^{13}C NMR (126 MHz, DMSO, δ from solvent) δ 172.61, 168.32, 137.54, 135.83, 131.09, 130.43, 122.18, 120.75, 51.18, 35.08, 28.50, 23.88, 20.99. LRMS-ESI (m/z): [M + H]$^+$ Theoretical for $C_{13}H_{15}NO_5$: 266.1; Experimental: 266.1.

methyl (*R*)-3-(2-((1-(naphthalen-1-yl)ethyl)carbamoyl)phenyl)propanoate (3). A 20 mL DCM solution containing 2-(3-methoxy-3-oxopropyl)benzoic acid (0.500 g, 2.4 mmol) was cooled to 0 ºC followed by addition of HBTU (1.138 g, 3.0 mmol). This solution was stirred for 30 min, followed by addition of (*R*)-1-(naphthalen-1-yl)ethan-1-amine (0.409 g, 2.4 mmol) and DIPEA (0.522 mL, 3.0 mmol). The solution was warmed to RT and stirred for 16 h. The reaction mixture was quenched with 50 mL of H_2O and extracted with DCM (3×50 mL). The organic layers were collected and dried with $MgSO_4$ and concentrated under reduced pressure. The residue was purified by silica gel chromatography using 3:1 Hexanes:EtOAc (R_f = 0.36) to afford a white solid. Washes were performed, and the resulting solid was dried under reduced pressure. This workup afforded the product as an off-white solid (0.723 g, 2.0 mmol, 83%). ^1H NMR (500 MHz, DMSO-d_6) δ from residual protio solvent 8.95 (d, J = 7.9 Hz, 1H), 8.24 (d, J = 8.4 Hz, 1H), 7.95 (d, J = 8.0 Hz, 1H), 7.84 (d, J = 8.1 Hz, 1H), 7.65 − 7.46 (m, 4H), 7.38 − 7.29 (m, 2H), 7.30 − 7.23 (m, 2H), 5.92 (p, J = 7.2 Hz, 1H), 3.57 (s, 3H), 2.92 (t, J = 8.0 Hz, 2H), 2.57 (t, J = 7.9 Hz, 2H), 1.58 (d, J = 6.9 Hz, 3H). ^{13}C NMR (126 MHz, DMSO, δ from solvent): 172.51, 168.02, 140.12, 138.11, 136.96, 133.36, 130.39, 129.56, 129.34, 128.62, 127.29, 127.19, 126.11, 126.00, 125.56, 125.43, 123.11, 122.46, 51.21, 44.36, 34.96, 27.96, 21.36. HRMS-ESI (m/z): [M + H]$^+$ Theoretical for $C_{23}H_{24}NO_3$: 362.1756; Experimental: 362.1745.

methyl (*R*)-3-(4-acetamido-2-((1-(naphthalen-1-yl)ethyl)carbamoyl)phenyl)propanoate (4). Compound **4** was prepared similarly to the amide coupling of **3**. The amount of materials used were: **2** (0.350 g, 1.08 mmol); HBTU (0.899 g, 2.15 mmol); (*R*)-1-(naphthalen-1-yl)ethan-1-amine (0.366 g, 2.15 mmol) and DIPEA (0.749 mL, 4.30 mmol). Silica gel column purification was performed under a gradient from 1:1, 2:1, 3:1 EtOAc:Hexanes at 1 column volume for each gradient step. Compound **4** was isolated as white solid (0.410 g, 0.980 mmol, 91%). ^1H NMR (500 MHz, DMSO-d_6, δ from residual protio solvent) δ 9.96 (s, 1H),

8.95 (d, J = 8.0 Hz, 1H), 8.24 (d, J = 8.4 Hz, 1H), 7.95 (dd, J = 8.0, 1.6 Hz, 1H), 7.84 (d, J = 8.2 Hz, 1H), 7.64 − 7.55 (m, 3H), 7.54 (ddd, J = 8.1, 6.8, 1.3 Hz, 1H), 7.52 − 7.45 (m, 2H), 7.17 (d, J = 8.4 Hz, 1H), 5.92 (p, J = 7.2 Hz, 1H), 3.56 (s, 3H), 2.83 (t, J = 7.8 Hz, 2H), 2.69 (s, 3H), 2.53 (t, J = 8.0 Hz, 2H), 2.02 (s, 3H), 1.57 (d, J = 6.9 Hz, 3H). ^{13}C NMR (126 MHz, DMSO, δ from solvent) δ 172.50, 168.22, 167.88, 140.07, 137.33, 137.26, 133.33, 132.26, 130.39, 129.78, 128.60, 127.19, 126.14, 125.56, 125.36, 123.08, 122.39, 119.69, 117.71, 51.17, 44.22, 38.19, 35.02, 27.39, 23.85, 21.39. LRMS-ESI (m/z): [M + H]$^+$ Theoretical for $C_{25}H_{26}N_2O_4$: 419.2; Experimental: 419.2.

(*R*)-2-(3-hydrazineyl-3-oxopropyl)-*N*-(1-(naphthalen-1-yl)ethyl)benzamide (5). To a 10 mL EtOH solution containing **1** (0.400 g, 1.11 mmol) was added 0.5 mL (~1 M) of hydrazine monohydrate (N_2H_4 64-65%, reagent grade 95%). The pale-yellow, homogenous solution was refluxed for 16 h. The resulting solution was reduced under vacuum to afford an off-white powder. To remove excess hydrazine monohydrate, several (3×15 mL) Et_2O washes were performed, and the resulting solid was dried under reduced pressure. This workup afforded the product as an off-white solid (0.390 g, 1.08 mmol, 97%). ^{1}H NMR (500 MHz, DMSO-d_6, δ from residual protio solvent): 8.97 (d, J = 7.9 Hz, 1H), 8.91 (s, 1H), 8.25 (d, J = 8.5 Hz, 1H), 7.96 (d, J = 8.1 Hz, 1H), 7.84 (d, J = 8.1 Hz, 1H), 7.65 (d, J = 7.2 Hz, 1H), 7.61 (t, J = 7.6 Hz, 1H), 7.54 (dt, J = 15.0, 7.6 Hz, 2H), 7.35 (t, J = 7.4 Hz, 1H), 7.31 (d, J = 7.4 Hz, 1H), 7.28 − 7.21 (br, 2H), 5.93 (p, J = 7.2 Hz, 1H), 4.21 (s, 2H), 2.91 (td, J = 7.5, 4.3 Hz, 2H), 2.35 (t, J = 7.9 Hz, 2H), 1.60 (d, J = 6.9 Hz, 3H). ^{13}C NMR (126 MHz, DMSO, δ from solvent): 170.82, 168.04, 140.20, 138.74, 137.05, 133.35, 130.37, 129.22, 129.20, 128.61, 127.21, 127.16, 126.14, 125.72, 125.55, 125.50, 123.12, 122.46, 44.42, 34.85, 28.22, 21.44. HRMS-ESI (m/z): [M + H]$^+$ Theoretical for $C_{22}H_{24}N_3O_2$: 362.1859; Experimental: 362.1885.

(*R*)-5-acetamido-2-(3-hydrazineyl-3-oxopropyl)-*N*-(1-(naphthalen-1-yl)ethyl)benzamide (6). Compound **6** was prepared analogously to **5**. The amounts of materials used were: **4** (0.400 g, 0.956 mmol); 10 mL EtOH solution containing; 0.5 mL (~1M) of hydrazine monohydrate (N_2H_4 64-65%, reagent grade 95%). This procedure afforded an off-white solid (0.388 g, 0.927 mmol, 97%) (^{1}H NMR (500 MHz, DMSO-d_6, δ from residual protio solvent) δ 9.94 (s, 1H), 8.97 (d, J = 7.9 Hz, 1H), 8.89 (s, 1H), 8.24 (d, J = 8.4 Hz, 1H), 7.95 (d, J = 8.1 Hz, 1H), 7.84 (d, J = 8.0 Hz, 1H), 7.65 − 7.56 (m, 3H), 7.53 (dt, J = 18.1, 7.5 Hz, 2H), 7.45 (s, 1H), 7.15 (d, J = 8.4 Hz, 1H), 5.92 (p, J = 6.9 Hz, 1H), 4.11 (s, br, 2H), 2.82 (hept, J = 7.5, 7.0 Hz, 2H), 2.31 (t, 2H), 2.01 (s, 3H), 1.58 (d, J = 7.0 Hz, 3H). ^{13}C NMR (126 MHz, DMSO, δ from solvent) δ 170.85, 168.18, 167.90, 140.17, 137.40, 137.02, 133.34, 132.89, 130.39, 129.42, 128.60, 127.18, 126.17, 125.57, 125.44, 123.11, 122.39, 119.68, 117.66, 44.31, 34.89, 27.65, 23.85, 21.48. LRMS-ESI (m/z): [M + H]$^+$ Theoretical for $C_{25}H_{26}N_4O_3$: 419.2; Experimental: 419.2.

Preparation of compounds with electrophilic warheads. Compounds **7**, **9**, **11**, and **13** were prepared by taking 0.030 g (0.083 mmol) of **5** and 0.029 mL (0.166 mmol) of DIPEA into 5 mL anhydrous DCM under N_2 atmosphere. Once dissolved, 0.100 mmol (1.2 equiv.) of appropriate acid chloride was added while stirring under N_2 atmosphere. Rapid reaction resulted in precipitation of a white solid. The reaction was left at RT for 2 h with no observable changes. The DCM was removed under reduced pressure and Et_2O

was added to the remaining residue to precipitate a white solid that was collected with a 2 mL fritted glass funnel. The remaining white solid was washed extensively with Et_2O, dried, and collected. Isolated yields: **7** (0.022 g, 0.046 mmol, 56%); **9** (0.018 g, 0.041 mmol, 50%); **11** (0.020 g, 0.047 mmol, 56%); **13** (0.024 g, 0.050 mmol, 60%).

Compounds **8** and **10** were prepared by placing 0.040 g (0.096 mmol) of **6** in 5 mL of anhydrous DMF followed by addition of K_2CO_3 (0.020 g, 0.145 mmol). The solution was stirred while 0.115 mmol (1.2 equiv.) of appropriate acid chloride was added. The solution was stirred at RT for 2 h followed by addition of 25 mL EtOAc and extraction with 3×25 mL of H_2O to remove DMF. The organic layers were combined, dried with $MgSO_4$, and concentrated under reduced pressure. The crude residue was purified by silica gel flash chromatography using pure EtOAc with 1-5% MeOH to yield white solids: **8** (0.016 g, 0.032 mmol, 34%); **10** (0.019 g, 0.036 mmol, 37%).

methyl(R,E)-4-(2-(3-(2-((1-(naphthalen-1 yl)ethyl)carbamoyl)phenyl)propanoyl)hydrazineyl)-4-oxobut-2-enoate (7). ^1H NMR (500 MHz, DMSO-d_6, δ from residual protio solvent) δ 10.53 (s, 1H), 10.16 (s, 1H), 8.93 (d, J = 7.9 Hz, 1H), 8.24 (d, J = 8.6 Hz, 1H), 7.95 (d, J = 8.1 Hz, 1H), 7.83 (d, J = 8.2 Hz, 1H), 7.67 − 7.57 (m, 2H), 7.56 − 7.48 (m, 2H), 7.39 − 7.21 (m, 4H), 7.08 (d, J = 15.6 Hz, 1H), 6.69 (dd, J = 15.5, 1.9 Hz, 1H), 5.93 (p, J = 7.3 Hz, 1H), 3.75 (s, 3H), 2.94 (dt, J = 8.8, 5.0 Hz, 2H), 2.55 − 2.47 (m, 3H *overlaps with DMSO-d_6*), 1.59 (d, J = 6.9 Hz, 3H). ^{13}C NMR (126 MHz, DMSO, δ from solvent) δ 170.30, 168.56, 165.73, 161.57, 140.66, 139.06, 137.56, 135.58, 133.86, 130.91, 129.90, 129.82, 129.77, 129.13, 127.73, 127.70, 126.67, 126.35, 126.08, 126.02, 123.65, 122.96, 52.59, 44.94, 35.14, 28.56, 21.92. HRMS-ESI (*m/z*): [M + H]$^+$ Theoretical for $C_{27}H_{28}N_3O_5$: 474.2029; Experimental: 474.2007.

methyl-(R,E)-4-(2-(3-(4-acetamido-2-((1-(naphthalen-1-yl)ethyl)carbamoyl)phenyl)propanoyl)hydrazineyl)-4-oxobut-2-enoate (8). ^1H NMR (500 MHz, DMSO-d_6, δ from residual protio solvent) δ 10.52 (s, 1H), 10.15 (s, 1H), 9.95 (s, 1H), 8.93 (d, J = 7.9 Hz, 1H), 8.24 (d, J = 8.6 Hz, 1H), 7.95 (d, J = 8.0 Hz, 1H), 7.83 (d, J = 8.2 Hz, 1H), 7.64 − 7.57 (m, 3H, 7.56 − 7.48 (m, 2H), 7.45 (s, 1H), 7.21 (d, J = 8.4 Hz, 1H), 7.07 (d, J = 15.6 Hz, 1H), 6.68 (d, J = 15.5 Hz, 1H), 5.93 (p, J = 7.2 Hz, 1H), 3.75 (s, 3H), 2.86 (m, 2H), 2.47 (m, 2H), 2.02 (s, 3H), 1.57 (d, J = 6.9 Hz, 3H). ^{13}C NMR (126 MHz, DMSO, δ from solvent) δ 169.79, 168.17, 167.88, 165.18, 161.03, 140.09, 137.38, 137.09, 135.02, 133.31, 132.65, 130.37, 129.57, 129.22, 128.57, 127.17, 126.16, 125.55, 125.41, 123.09, 122.34, 119.68, 117.60, 52.04, 44.27, 34.64, 27.45, 23.83, 21.41. HRMS-ESI (*m/z*): [M + H]$^+$ Theoretical for $C_{29}H_{31}N_4O_6$: 531.2244; Experimental: 531.2217.

(R)-2-(3-(2-(2-chloroacetyl)hydrazineyl)-3-oxopropyl)-N-(1-(naphthalen-1-yl)ethyl)benzamide (9). ^1H NMR (500 MHz, DMSO-d_6, δ from residual protio solvent) δ 10.21 (s, 1H), 9.98 (s, 1H), 8.95 (d, J = 7.8 Hz, 1H), 8.24 (d, J = 8.5 Hz, 1H), 7.96 (d, J = 8.1 Hz, 1H), 7.84 (d, J = 8.1 Hz, 1H), 7.67 − 7.49 (m, 4H), 7.38 − 7.23 (m, 4H), 5.93 (p, J = 7.2 Hz, 1H), 4.14 (s, 2H), 2.94 (t, J = 9.1, 2H), 2.48 (t, J = 9.1 Hz, 2H), 1.60 (d, J = 6.8

Hz, 3H). ^{13}C NMR (126 MHz, DMSO, δ from solvent) δ 170.08, 168.06, 164.65, 140.15, 138.56, 137.04, 133.35, 130.39, 129.39, 129.31, 128.62, 127.20 (two overlapping ^{13}C signals), 126.16, 125.83, 125.58, 125.51, 123.14, 122.45, 44.43, 40.86, 34.62, 28.02, 21.41 HRMS-ESI (*m/z*): [M + H]$^+$ Theoretical for $C_{24}H_{25}ClN_3O_3$: 438.1584; Experimental: 438.1565.

(*R*)-5-acetamido-2-(3-(2-(2-chloroacetyl)hydrazineyl)-3-oxopropyl)-*N*-(1-(naphthalen-1-yl)ethyl)benzamide (10).

^{1}H NMR (500 MHz, DMSO-d_6, δ from residual protio solvent) δ 10.20 (s, 1H), 9.96 (s, 2H), 8.94 (d, *J* = 8.0 Hz, 1H), 8.25 (d, *J* = 8.5 Hz, 1H), 7.96 (d, *J* = 8.1 Hz, 1H), 7.85 (d, *J* = 8.2 Hz, 1H), 7.62 (q, *J* = 6.7 Hz, 3H), 7.54 (m, 2H), 7.46 (s, 1H), 7.21 (d, *J* = 8.4 Hz, 1H), 5.93 (q, *J* = 7.3 Hz, 1H), 4.14 (s, 2H), 2.86 (m, 2H), 2.45 (t, *J* = 7.9 Hz, 2H), 2.03 (s, 3H), 1.58 (d, *J* = 6.8 Hz, 3H). ^{13}C NMR (126 MHz, DMSO, δ from solvent) δ 170.60, 168.72, 168.43, 165.14, 140.64, 137.92, 137.63, 133.86, 133.21, 130.92, 130.12, 129.12, 127.72, 126.71, 126.10, 125.97, 123.64, 122.89, 120.23, 118.13, 44.82, 41.37, 35.18, 27.97, 24.38, 21.96. HRMS-ESI (*m/z*): [M + H]$^+$ Theoretical for $C_{26}H_{28}ClN_4O_4$: 495.1799; Experimental: 495.1788.

(*R*)-2-(3-(2-(2-cyanoacetyl)hydrazineyl)-3-oxopropyl)-*N*-(1-(naphthalen-1-yl)ethyl)benzamide (11).

^{1}H NMR (500 MHz, DMSO-d_6, δ from residual protio solvent) δ 10.16 (s, 1H), 9.96 (s, 1H), 8.93 (d, *J* = 7.8 Hz, 1H), 8.23 (d, *J* = 8.5 Hz, 1H), 7.95 (d, *J* = 8.2 Hz, 1H), 7.83 (d, *J* = 8.2 Hz, 1H), 7.66 − 7.57 (m, 2H), 7.57 − 7.48 (m, 2H), 7.39 − 7.21 (m, 4H), 5.92 (p, *J* = 7.1 Hz, 1H), 3.74 (s, 2H), 2.97 − 2.89 (t, 7.6 Hz, 2H), 2.47 (t, *J* = 7.6 Hz, 2H), 1.59 (d, *J* = 6.9 Hz, 3H). ^{13}C NMR (126 MHz, DMSO, δ from solvent) δ 170.13, 168.03, 161.12, 140.14, 138.52, 137.02, 133.34, 130.39, 129.39, 129.29, 128.61, 127.20, 127.18, 126.15, 125.82, 125.57, 125.50, 123.13, 122.44, 115.62, 44.41, 34.55, 27.99, 23.67, 21.39. HRMS-ESI (*m/z*): [M + H]$^+$ Theoretical for $C_{25}H_{25}N_4O_3$: 429.1928; Experimental: 429.1949.

(*R*)-*N*-(1-(naphthalen-1-yl)ethyl)-2-(3-oxo-3-(2-propioloylhydrazineyl)propyl)benzamide (12).

Compound **12** was synthesized under the same conditions as compounds **7**, **9**, **11**, and **13** except the initial coupling to the hydrazide of **5** was achieved with 3-(trimethylsilyl)propioloyl chloride. The DCM was removed under reduced pressure and the crude material was immediately dissolved in 1:1 THF:MeOH (6 mL total volume) and 10 mg of K_2CO_3 was added. The solution was stirred and monitored by TLC until the reaction was complete, approximately 30 min. The solution was concentrated and purified by silica gel flash chromatography (2:1 EtOAc:Hexanes) to yield 8 mg (0.019 mmol, 23%) of a pale yellow solid. ^{1}H NMR (500 MHz, Acetone-d_6, δ from residual protio solvent) δ 9.49 (s, 1H), 9.12 (s, 1H), 8.33 (d, *J* = 8.6 Hz, 1H), 8.05 (d, *J* = 8.2 Hz, 1H), 7.93 (d, *J* = 8.2 Hz, 1H), 7.83 (d, *J* = 8.2 Hz, 1H), 7.72 (d, *J* = 7.2 Hz, 1H), 7.63 (t, *J* = 7.8 Hz, 1H), 7.52 (m, 2H), 7.40 − 7.28 (m, 3H), 7.19 (m, 1H), 6.12 (p, *J* = 7.3 Hz, 1H), 3.14 − 3.00 (m, *J* = 7.4 Hz, 2H), 2.79 (s, 1H), 2.64 (m, 2H), 1.74 (d, *J* = 6.8 Hz, 3H). ^{13}C NMR (126 MHz, Acetone, δ from solvent) δ 171.42, 169.30, 151.76, 140.76, 140.01, 138.07, 134.97, 132.12, 130.72, 130.42, 129.63, 128.52, 128.23, 127.15, 126.83, 126.52, 126.35, 124.37, 123.62, 79.90, 77.04, 76.70, 45.67, 36.17, 21.58. HRMS-ESI (*m/z*): [M + H]$^+$ Theoretical for $C_{25}H_{24}N_3O_3$: 414.1819; Experimental: 414.1852.

(R)-2-(3-(2-(2-cyano-3-cyclopropylacryloyl)hydrazineyl)-3-oxopropyl)-N-(1-(naphthalen-1-yl)ethyl)benzamide (13). ^{1}H NMR (500 MHz, Acetone-d_6, δ from residual protio solvent) δ 8.32 (d, J = 8.6 Hz, 1H), 7.99 − 7.91 (m, 2H), 7.83 (d, J = 8.3 Hz, 1H), 7.71 − 7.68 (m, 2H), 7.63 − 7.58 (m, 1H), 7.57 − 7.46 (m, 2H), 7.39 (m, 1H), 7.32 (m, 2H), 7.21 (t, J = 7.1 Hz, 1H), 6.10 (p, J = 7.5 Hz, 1H), [1:2.5 *E:Z* isomer ratio; 4.51 (dd, J = 25.6, 7.6 Hz); 4.24 (dd, J = 54.2, 11.8 Hz, 1H)], 3.21 − 2.98 (m, 4H), 2.77 (s, 1H), 1.73 (d, J = 6.9 Hz, 3H), 1.18 − 1.02 (m, 1H), 0.70 − 0.56 (m, 2H), 0.56 − 0.41 (m, 2H). Many multiple peaks with close δ spacings were observed in the ^{13}C NMR presumably due to the *E:Z* isomer mixture, these values are reported as observed. ^{13}C NMR (126 MHz, Acetone-d_6, δ from solvent) δ 169.39, 169.21, 169.17, 169.15, 169.11, 169.06, 166.20, 166.09, 140.81, 140.80, 140.06, 140.05, 140.03, 139.99, 138.12, 138.09, 134.96, 132.10, 132.08, 131.02, 131.00, 130.47, 130.45, 129.68, 129.65, 128.53, 128.51, 128.50, 128.17, 128.14, 127.12, 127.11, 126.91, 126.51, 126.37, 126.32, 124.33, 124.31, 123.53, 123.49, 123.47, 115.74, 115.72, 114.81, 114.79, 64.23, 59.93, 45.69, 45.65, 45.62, 43.16, 43.13, 43.02, 42.97, 39.15, 39.11, 39.07, 30.30, 30.15, 29.99, 29.84, 29.69, 29.53, 29.38, 29.10, 28.56, 28.54, 21.64, 21.60, 12.09, 12.05, 12.02, 3.47, 3.23, 3.20, 2.90, 2.13, 2.10. HRMS-ESI (*m/z*): [M + H]$^+$ Theoretical for $C_{29}H_{29}N_4O_3$: 481.2240; Experimental: 481.2289.

Preparation of noncovalent derivatives of GRL0617. Compounds **14** and **15** were prepared analogously to the amide coupling of **3**. The amount of materials used were: 2-methylbenzoic acid (0.250 g, 1.80 mmol); 5-acetamido-2-methylbenzoic acid (0.348 g, 1.80 mmol); HBTU (0.853 g, 2.25 mmol); (R)-1-(naphthalen-1-yl)ethan-1-amine (0.306 g, 1.80 mmol) and DIPEA (0.392 mL, 2.25 mmol). Silica gel column purification was performed on **14** (3:1 Hexanes:EtOAc) and **15** (5% MeOH in DCM) to yield white solids **14** (0.463 g, 1.61 mmol, 89%); **15** (0.519 g, 1.50 mmol, 83%).

(R)-2-methyl-N-(1-(naphthalen-1-yl)ethyl)benzamide (14). ^{1}H NMR (500 MHz, DMSO-d_6, δ from residual protio solvent) δ 8.86 (d, J = 8.0 Hz, 1H), 8.25 (d, J = 8.4 Hz, 1H), 7.96 (d, J = 8.0 Hz, 1H), 7.85 (d, J = 8.1 Hz, 1H), 7.66 − 7.49 (m, 4H), 7.35 − 7.28 (m, 2H), 7.25 − 7.19 (m, 2H), 5.93 (p, J = 7.2 Hz, 1H), 2.30 (s, 3H), 1.59 (d, J = 6.9 Hz, 3H). ^{13}C NMR (126 MHz, DMSO, δ from solvent)) δ 168.09, 140.25, 137.22, 135.01, 133.35, 130.40, 130.23, 129.07, 128.62, 127.18, 126.96, 126.08, 125.55, 125.43, 125.36, 123.17, 122.49, 44.26, 21.42, 19.21. HRMS-ESI (*m/z*): [M + H]$^+$ Theoretical for $C_{20}H_{20}NO$: 290.1545; Experimental: 290.1594.

(R)-5-acetamido-2-methyl-N-(1-(naphthalen-1-yl)ethyl)benzamide (15). ^{1}H NMR (500 MHz, DMSO-d_6, δ from residual protio solvent) δ 9.91 (s, 1H), 8.85 (d, J = 8.1 Hz, 1H), 8.24 (d, J = 8.5 Hz, 1H), 7.96 (dd, J = 8.1, 1.6 Hz, 1H), 7.84 (d, J = 8.2 Hz, 1H), 7.64 − 7.45 (m, 7H), 7.12 (d, J = 8.3 Hz, 1H), 5.92 (p, J = 7.1 Hz, 1H), 3.29 (s, 1H), 2.69 (s with broadened couplings, 3H), 2.21 (s, 3H), 2.01 (d, J = 1.7 Hz, 3H), 1.57 (d, J = 6.9 Hz, 3H), 1.19 (s, 1H). ^{13}C NMR (126 MHz, DMSO, δ from solvent) δ 168.12, 167.96, 140.20, 137.52, 136.78, 133.33, 130.40, 130.38, 129.10, 128.59, 127.18, 126.10, 125.55, 125.37, 123.15, 122.42, 119.51, 117.50, 44.15, 38.19, 23.84, 21.44, 18.51. HRMS-ESI (*m/z*): [M + H]$^+$ Theoretical for $C_{22}H_{23}N_2O_2$: 369.1579; Experimental: 369.1555.

Protein expression and purification. PLpro from SARS-CoV-2 was produced using a previously described procedure with minor modifications,[51] which we summarize here. First, the protein was expressed using *E. coli* BL21(DE3) cells that had been transformed with a pMCSG92 expression plasmid, which includes a T7 promoter and TEV protease-cleavable C-terminal 6xHis tag. Cells were plated on LB agar and cultivated in a shaking incubator (250 rpm) at 37°C in Lysogeny Broth medium (Lennox recipe) using 1 L per baffled 2.8 L Fernbach flask. Carbenicillin was used for antibiotic selection throughout. Bacterial growth was monitored by measuring the absorbance at 600 nm (OD_{600}). Upon reaching an OD_{600} of ~0.7, the incubator temperature was set to 18 °C and isopropyl β-D-1-thiogalactopyranoside (IPTG) was added to 0.2 mM. After approximately 18 hours, the culture was harvested by centrifugation at 6000×g for 30 minutes. After decanting off the supernatant, the pellets were stored at -80°C until needed for protein purification.

A cell pellet harvested from a 1 L culture was thawed and resuspended in 100 mL of lysis buffer containing 50 mM HEPES, 300 mM NaCl, 50 mM imidazole, 5% glycerol, and 1 mM TCEP at pH 7.4. Following resuspension, the cells were subjected to tip sonication on ice at 50% amplitude (2 seconds on and 10 seconds off) for a total sonication time of 5 minutes using a Branson 450D Digital Sonifier. After clarifying the lysate by 38,500xg centrifugation for 35 minutes at 4°C, the decanted supernatant was passed through 1.6- and 0.45-micron syringe filters sequentially and kept on ice while loading a 5-mL HisTrap HP column (Cytiva) at 2 mL/min. After washing the column with 10 column volumes (CV) of lysis buffer, partially purified PLpro was eluted using a linear gradient (20 CVs) of lysis buffer with 500 mM imidazole. Elution fractions (2 mL) were collected and PLpro was identified using SDS-PAGE on a 4-20% Mini-Protean TGX Stain-Free protein gel (Bio-Rad). Pooled fractions containing PLpro were dialyzed overnight at 6°C in 50 mM HEPES pH 7.4 with 150 mM NaCl, 5% glycerol, 20 mM imidazole, and 1 mM TCEP in the presence of His-tagged TEV protease (1 mg TEV protease:100 mg PLpro). After confirming His-tag cleavage by SDS-PAGE, the dialyzed protein solution was passed over a 5-mL HisTrap HP column to remove His-tagged impurities. The column flowthrough was collected, evaluated with SDS-PAGE, and concentrated with a 10-kDa molecular weight cutoff Amicon Ultra15 ultrafiltration membrane. Upon concentration, partially purified protein was applied at 0.5 mL/min to a Superdex 75 10/300 GL size-exclusion column (Cytiva) that had been equilibrated with 50 mM Tris HEPES pH 7.4 with 150 mM NaCl, 5% glycerol, and 1 mM TCEP. Fractions (0.5 mL) containing purified PLpro were collected, pooled, and concentrated for further use.

PLpro inhibition assays. The assays were performed in 40 μL total volume in black half area 96-well plates (Greiner PN 675076) at 25°C. The assay buffer contained 20 mM Tris-HCl pH 7.45, 0.1 mg/mL bovine serum albumin fraction V, and 2 mM reduced glutathione. The final DMSO concentration in all assays was 2.5% v/v. PLpro initial rates were measured using a previously established fluorogenic peptide substrate assay.[15, 22, 23] The substrates Z-LRGG-AMC and Z-RLRGG-AMC were purchased from Bachem (PN 4027157 and 4027158), dissolved to 10 mM in DMSO and stored in aliquots at -20 °C. To determine Michaelis-Menten parameters, 20 μL enzyme solution was dispensed into wells (250 nM final concentration), and reactions were initiated by adding 20 μL substrate to 0-500 μM final concentration, in

triplicate. Release of aminomethylcoumarin (AMC) was monitored by a Biotek Synergy H1 fluorescence plate reader every 50 s with an excitation wavelength of 345 nm and an emission wavelength of 445 nm, 6.25 mm read height, and gain = 60. After background subtraction of the average of no-enzyme negative controls, product formation was quantified using a 0.02–5 µM calibration curve of AMC (Sigma PN 257370). Initial rates were determined for time points in the initial linear range by linear regression in Excel, and GraphPad Prism 9 was used to perform nonlinear regression of the Michaelis-Menten equation to the initial rate vs. substrate concentration data to yield K_M and V_{max}.

Inhibitors were characterized by dispensing 10 µL enzyme solution into wells (115 nM final concentration), followed by 10 µL inhibitor solution at 4X desired final concentrations in 5% v/v DMSO in at least duplicate, centrifuging briefly, and incubating for 30 min. Reactions were initiated by adding 20 µL substrate to 100 µM final concentration. Initial rates were determined as described above and % residual activities were determined by normalizing to the average of no inhibitor controls (100% activity). Thirty-minute IC_{50} values were determined by nonlinear regression to the [Inhibitor] vs. normalized response – Variable slope equation using GraphPad Prism 9.

Time-dependent inhibition assays were performed as described above, except that preincubation times were varied by adding the inhibitor to the enzyme at specific time points. For each inhibitor concentration, initial rates were normalized such that 0 preincubation time is 100% and plotted against preincubation time. A nonlinear regression to a one phase decay model was performed to determine the rate constants k_{obs} for each concentration and their 95% confidence intervals. These rate constants were then plotted against inhibitor concentration, and the data in the initial linear region was fit to determine the slope, which is k_{inact}/K_I. All regressions were performed with GraphPad Prism 9.

Inhibition of full-length Nsp3 de-ISG15ylase activities. HEK293T cells were grown in 10 cm dishes and transiently transfected with pEF-HA-Nsp3 or pEF empty vector using lipofectamine 3000 (Thermo Fisher). 24 hrs after transfection, cells were harvested and lysed in 1% NP-40 lysis buffer (50 mM Tris-HCl, pH 7.5, 150 mM NaCl, 10% glycerol, 1% NP-40, 1 mM phenylmethylsulfonyl fluoride (PMSF)). Full-length HA-Nsp3 was purified using anti-HA immunoprecipitation, washed 4 times using the lysis buffer and the Nsp3 containing beads (~100 ml bead volume) were resuspended in 1.0 ml enzyme assay buffer (20 mM Tris-HCl, pH 8.0, 0.05% CHAPS, 2 mM b-mercaptoethanol). 20 ml of the immunoprecipitated Nsp3 beads and the whole cell lysates (30 mg) were run on 8% SDS-PAGE, transferred to PVDF membrane, and probed with anti-HA antibody to detect full length Nsp3. Activity of Nsp3 on the bead (5.0 ml) was monitored using ISG15-CHOP2 substrate (20 nM) in the presence of DMSO as vehicle or dose range of compounds in DMSO. Percent inhibition was calculated using the formula,

% Inhibition = 100 x [1 - (X - LOW)/(HIGH - LOW)]

where X is the signal at a given concentration of inhibitor, LOW is the signal with no DUB added (100% inhibition) and HIGH is the signal with DUB in the presence of DMSO (0% inhibition). Percent inhibition was plotted using GraphPad Prism and IC_{50} values were determined using nonlinear regression to the [Inhibitor] vs. normalized response – Variable slope equation using GraphPad Prism 9.

Mass spectrometry to assess covalent adduct formation. A Waters Synapt HDMS QTOF mass spectrometer was used to measure the intact protein mass of PLpro with and without preincubation with inhibitors to detect covalent adduct formation. To prepare the samples, 2 µL of 20 mM inhibitor stocks in DMSO were added to 100 µL PLpro at 1 mg/mL concentration and incubated 1 h at room temperature. Previously described protocols for ultrafiltration and denaturing direct infusion[52] were implemented as follows. Samples were processed by ultrafiltration with a Vivaspin 500 10 kDa PES membrane by diluting the sample to 0.5 mL with 10 mM LC-MS grade ammonium acetate and reducing volume to 50 µL twice, followed by the same procedure with 2.5 mM ammonium acetate. Protein concentrations were estimated by A280 with a NanoDrop 2000, and samples were diluted to 2 mg/mL in 2.5 mM ammonium acetate, and then 10 µL were further diluted into 90 µL 50:50 acetonitrile:water with 0.1% formic acid. Sample was introduced into the electrospray ionization source by syringe pump at a flow rate of 10 µL/min and MS1 spectra were collected for m/z 400-1500, 5 s/scan, for 1 min. The protein monoisotopic mass was determined from the averaged spectra using mMass 5.5.[53]

Inhibition of PLpro deubiquitinase and de-ISG15ylase activities and deubiquitinase selectivity. Candidate inhibitors were assayed by LifeSensors, Inc. (Malvern, PA) in quadruplicate for inhibition of SARS-CoV-2 PLpro with Ub-rhodamine or ISG15-CHOP2 and with human deubiquitinase (DUB) enzymes, including USP30, USP15, USP8, USP7, USP4, and USP2C as well as UCHL1 with Ub-rhodamine, except for USP7, which was tested with Ub-CHOP2. The CHOP assay[54] uses a quenched enzyme platform to quantify the DUB inhibition activity of the compounds. In this assay, a reporter enzyme is fused to the C-terminus of ubiquitin. The reporter is silent when fused to ubiquitin but becomes fluorescent upon cleavage from the C-terminus by a DUB. Thus, measurement of the reporter activity is a direct measure of DUB activity. Assays were performed with a positive control (PR619) and negative control (i.e., without the inhibitor). DUBs at previously optimized concentrations were used with previously optimized suitable DUB substrates to evaluate inhibitory activity. Briefly, the received compounds in DMSO were thawed before use and simultaneously aliquoted to protect against deterioration from freeze-thaw cycles. Compounds were diluted at desired fold to measure a dose response curve in DMSO. DMSO control was used as 0% inhibition in the presence of DUB and the DMSO control without the DUB was considered as the 100% inhibition control to calculate IC_{50} values. Dose response-inhibition curves were plotted in GraphPad Prism with log-transformed concentration on the X-axis with percentage inhibition (30 min time point) on the Y-axis using log [inhibitor] versus the response-variable slope. The selectivity index (SI) is the fold change in selectivity for PLpro compared to the DUB inhibition activity of other DUBs in the selectivity panel.

–

PLpro expression, purification, and crystallization. Wild-type PLpro from SARS-CoV-2 was expressed in BL21(DE3) *E. coli* cells transformed with the pMCSG53 expression plasmid with a T7 promoter and a TEV-cleavable, N-terminal 6xHis-tagged PLpro. *E. coli* cells were grown in LB media containing 50 μg/mL ampicillin at 37 °C in a shaking incubator (200 rpm) until the optical density (OD_{600}) of the culture was 0.6. The culture was then induced with 0.5 mM IPTG (GoldBio, USA) and grown for 16 hours at 18 °C. The culture was centrifuged for 15 min at 3000x g and the cells were obtained as pellets. *E. coli* pellets were resuspended in lysis buffer (50 mM HEPES pH 7.2, 150 mM NaCl, 5% glycerol, 20 mM imidazole, 10 mM 2-mercaptoethanol) and subjected to sonication for cell lysis. The soluble fraction of the whole cell lysate was separated by centrifugation at 20442×g for 80 minutes and was loaded onto a Ni-NTA Agarose (Qiagen, USA) gravity column pre-equilibrated with lysis buffer. The column was washed with 25 column volumes of wash buffer (50 mM HEPES pH 7.2, 150 mM NaCl, 5% glycerol, 50 mM imidazole, 10 mM 2-mercaptoethanol) and eluted in fractions with elution buffer (50 mM HEPES pH 7.2, 150 mM NaCl, 5% glycerol, 500 mM imidazole, 10 mM 2-mercaptoethanol). Fractions containing PLpro protein as determined by SDS-PAGE were combined and dialyzed overnight in dialysis buffer (50 mM HEPES pH 7.2, 150 mM NaCl, 5% glycerol, 10 mM 2-mercaptoethanol). Dialyzed PLpro was mixed with 6xHis-tagged TEV protease in 25:1 ratio, incubated overnight at 4 °C and was passed through Ni-NTA Agarose (Qiagen, USA) gravity column pre-equilibrated with dialysis buffer (50 mM HEPES pH 7.2, 150 mM NaCl, 5% glycerol, 10 mM 2-mercaptoethanol) to remove 6xHis-tagged impurities and TEV protease. Tagless PLpro obtained as the flowthrough was flash frozen and stored at -80 °C. All extraction and purification steps were performed at 4 °C. Reaction of tag-less PLpro in 20 mM Tris HCl pH 8.0 and 5 mM NaCl with a 10-fold molar excess of compound **7** was performed at 37 °C for 20 minutes. The PLpro-compound **7** complex in a solution containing 20 mM Tris HCl, 100 mM NaCl and 10 mM DTT was then used for crystallization at a concentration of 8 mg/ml. Initial crystal hits were obtained by screening around 900 crystallization conditions by the sitting drop method. Diffraction-quality crystals were obtained from a well solution containing PEG-3350, $CaCl_2$, $CdCl_2$ and $CoCl_3$.

Data collection and structure determination. The diffraction data were collected at 100 K at the BL12-2 beamline of the Stanford Synchrotron Radiation Light Source using Pilatus 6M detectors. Crystals for the complex were cryo-cooled using the well solution supplemented with 20% ethylene glycol. Diffraction data from two crystals were collected with 360 degrees of data per crystal and 0.2 degrees oscillation per image. For each crystal, diffraction data were merged and processed with the XDS suite of programs.[55] The structures were solved by molecular replacement with AMoRE[56] using the coordinates of SARS-CoV-2 PLpro complexed with the tetrapeptide-based inhibitor VIR251 (PDB 6WX4[11]) as the search model. Iterative rounds of model building and refinement were performed with the programs COOT[57] and REFMAC.[58] The details of data collection and refinement for the higher resolution data (3.10 Å) are presented in **Extended Data Table S2**.

SARS-CoV-2 antiviral assays. Initial screening to measure cytopathic effect (CPE) protection for the 50% efficacy concentration (EC_{50}) and cytotoxicity (CC_{50}) was performed in the Regional Biocontainment Laboratory at the University of Tennessee Health Science Center using an assay based on African green

monkey kidney epithelial (Vero E6) cells in 384-well plates.[59] Each plate can evaluate five compounds in duplicate at seven concentrations to measure an EC_{50} and CC_{50}. Each plate included three controls: cells alone (uninfected control), cells with SARS-CoV-2 (infected control) for plate normalization, and remdesivir as a drug control. Cell viability was measured using the CellTiter-Glo Luminescent Cell Viability Assay (Promega). In brief, Vero E6 TMPRSS ACE2 cells were grown to ~90% confluency in 384-well plates and treated for 1 hr with compounds. Cells were infected at an MOI = 0.1 of SARS-CoV-2 isolate USA-WA1/2020.[60] After 48 h, the SARS-CoV-2-mediated CPE and cytotoxicity were assessed by measuring live cells using CellTiter-Glo. The selectivity index at 50% (SI_{50}) was then calculated from the EC_{50} and CC_{50} values. To ensure robust and reproducible signals, each 384-well plate was evaluated for its Z-score, signal to noise, signal to background, and coefficient of variation. This assay has been validated for use in high-throughput format for single-dose screening and is sensitive and robust, with Z values > 0.5, signal to background > 20, and signal to noise > 3.3. Antiviral activity and cytotoxicity were also assessed with compound in the presence of 2 μM CP-100356 and SARS-CoV-2. Following incubation for 48 hours at 5% CO_2 and 37°C, the percent cell viability was measured with CellTiterGlo. Signals were read with an EnVision® 2105 multimode plate reader. Cells alone (positive control) and cells plus virus (negative control) were set to 100% and 0% cell viability to normalize the data from the compound testing. Data were normalized to cells (100%) and virus (0%) plus cells. Each concentration was tested in duplicate.

Compounds were also tested against SARS-CoV-2 variants using Vero E6 cells at the Institute for Antiviral Research at Utah State University under a service contract sponsored by NIAID using methods described previously.[61] Confluent or near-confluent cell culture monolayers of Vero E6 cells were prepared in 96-well disposable microplates the day before testing. Cells were maintained in Modified Eagle Medium (MEM) supplemented with 5% fetal bovine serum (FBS). For antiviral assays the same medium was used but with FBS reduced to 2% and supplemented with 50 μg/ml gentamicin. Compounds were dissolved in DMSO, saline, or the diluent requested by the submitter. Less soluble compounds were vortexed, heated, and sonicated, and if they still did not go into solution were tested as colloidal suspensions. Each test compound was prepared at four serial log_{10} concentrations, usually 0.1, 1.0, 10, and 100 μg/ml or μM (per sponsor preference). Lower concentrations were used when insufficient compound was supplied. Five microwells were used per dilution: three for infected cultures and two for uninfected toxicity cultures. Controls for the experiment consisted of six microwells that were infected and not treated (virus controls) and six that were untreated and uninfected (cell controls) on every plate. A known active drug was tested in parallel as a positive control drug using the same method applied for test compounds. The positive control was tested with every test run.

Growth media was removed from the cells and the test compound was applied in 0.1 ml volume to wells at 2X concentration. Virus, normally at ~60 $CCID_{50}$ (50% cell culture infectious dose) in 0.1 ml volume, was added to the wells designated for virus infection. Medium devoid of virus was placed in toxicity control wells and cell control wells. Plates were incubated at 37 °C with 5% CO_2 until marked CPE (>80% CPE for most virus strains) was observed in virus control wells. The plates were then stained with 0.011%

neutral red for approximately two hours at 37ºC in a 5% CO_2 incubator. The neutral red medium was removed by complete aspiration, and the cells were rinsed 1X with phosphate buffered saline (PBS) to remove residual dye. The PBS was removed completely, and the incorporated neutral red was eluted with 50% Sorensen's citrate buffer/50% ethanol for at least 30 minutes. Neutral red dye penetrates living cells. Thus, the more intense the red color, the larger the number of viable cells are present in the wells. The dye content in each well was quantified using a spectrophotometer at 540 nm wavelength. The dye content in each set of wells was converted to a percentage of dye present in untreated control wells using a Microsoft Excel spreadsheet and normalized based on the virus control. The 50% effective EC_{50} concentrations and 50% cytotoxic (CC_{50}) concentrations were then calculated by regression analysis. The quotient of CC_{50} divided by EC_{50} gives the selectivity index (SI). Compounds showing SI values $\geq$10 were considered active.

To confirm antiviral activity of compounds in human cells, we evaluated the compounds against SARS-CoV2 variants using a Caco-2 virus yield reduction assay. This test was performed at the Institute for Antiviral Research of Utah State University under a service contract sponsored by NIAID and following the method described previously.[61] Briefly, near-confluent monolayers of Caco-2 cells were prepared in 96-well microplates the day before testing. Cells were maintained in MEM supplemented with 5% FBS. The test compounds were prepared at a serial dilution of concentrations. The antiviral activity was also assessed with the compound alone or in the presence of 2 µM CP-100356. Three microwells were used per dilution. Controls for the experiment consisted of six microwells that were infected and not treated (virus controls) and six that were untreated and uninfected (cell controls) on every plate. A known active drug was tested in parallel as a positive control drug using the same method as is applied for test compounds. The positive control was tested with every test run. Growth media was removed from the cells and the test compound applied in 0.1 ml volume to wells at 2X concentration. Virus, normally at ~60 $CCID_{50}$ (50% cell culture infectious dose) in 0.1 ml volume, was added to the wells designated for virus infection. Medium devoid of virus was placed in cell control wells. Plates were incubated at 37 °C with 5% CO_2. After sufficient virus replication occurs (3 days for SARS-CoV-2), a sample of supernatant was taken from each infected well (three replicate wells were pooled) and tested immediately for virus yield reduction (VYR) or held frozen at −80 °C for later virus titer determination.

The VYR test is a direct determination of how much the test compound inhibits virus replication. Virus yielded in the presence of test compound was titrated and compared to virus titers from the untreated virus controls. Titration of the viral samples (collected as described above) was performed by endpoint dilution. Serial 1/10 dilutions of virus were made and plated into four replicate wells containing fresh cell monolayers of Vero E6 cells. Plates were then incubated, and cells were scored for the presence or absence of virus after distinct CPE was observed, and the $CCID_{50}$ was calculated using the Reed−Muench method.[58] The 90% effective concentration (EC_{90}) is calculated by regression analysis by plotting the log_{10} of the inhibitor concentration versus log_{10} of virus produced at each concentration. EC_{90} values were calculated from data to compare to the concentration of drug compounds as measured in the

pharmacokinetic experiments. Drug concentrations in critical tissues above EC_{90} values were targeted (instead of EC_{50} values) as for clinically relevant applications.

Metabolic stability. Intrinsic clearance in human, Sprague-Dawley rat, and CD-1 mouse liver microsomes and S9 fractions were measured[62] in duplicate for compounds **7**, **9**, and **14** by Eurofins Panlabs (St. Charles, MO, USA). Imipramine, propranolol, terfenadine, and verapamil were used as reference compounds at a test concentration of 0.1 mM. In each experiment and if applicable, the respective reference compounds were tested concurrently with the test compounds, and the data were compared with historical values determined at Eurofins. The experiments were accepted in accordance with Eurofins validation Standard Operating Procedure. Metabolic stability, expressed as percent of the parent compound remaining, was calculated by comparing the peak area of the compound at the time point relative to that at time t_0. The concentration of each compound was 1 mM and the incubation time ranged from 0 to 60 min. The half-life ($T_{1/2}$) was estimated from the slope of the initial linear range of the logarithmic curve of compound remaining (%) versus time, assuming first-order kinetics. The apparent intrinsic clearance (CL_{int}, µL/min/mg) was then calculated according to the following formula:

$$CL_{int} = \frac{0.693}{T_{1/2}\,(\text{mg protein}/\mu L)}$$

Pharmacokinetics. PK profiling assays were performed by Eurofins Panlabs (St. Charles, MO, USA). Compound **7** was formulated in 10% dimethyl sulfoxide (DMSO)/30% polyethylene glycol (PEG) 400/10% Kolliphor® EL/50% water for injection (WFI) at 1 and 0.6 mg/mL for PO and IV, respectively. A dosing volume of 10 mL/kg was applied for PO and 5 mL/kg for IV. Male ICR mice weighing 22 ± 2 g were provided by BioLasco Taiwan (under Charles River Laboratories Licensee). Animals were acclimated for 3 days prior to use and were confirmed with good health. All animals were maintained in a hygienic environment with controlled temperature (20-24°C), humidity (30-70%) and 12 hours light/dark cycles. Free access to sterilized standard lab diet [MFG (Oriental Yeast Co., Ltd., Japan)] and autoclaved tap water were granted. All aspects of this work, including housing, experimentation, and disposal of animals were performed in general accordance with the Guide for the Care and Use of Laboratory Animals: Eighth Edition (National Academy Press, Washington, D. C., 2011) in an AAALAC-accredited laboratory animal facility. The animal care and use protocol was reviewed and approved by the IACUC at Pharmacology Discovery Services Taiwan, Ltd. Animals were euthanized by CO_2 for blood collection by cardiac puncture. Blood samples (300-400 µL) were collected in tubes coated with EDTA-K2, mixed gently, then kept on ice and centrifuged at 2,500 ×g for 15 minutes at 4°C, within 1 hour of collection. The plasma was then harvested and kept frozen at -70°C until further processing.

The exposure levels (ng/mL) of **7** in plasma samples were determined by LC-MS/MS. Plots of plasma concentrations (mean ± SD) vs. time for **7** were constructed. The fundamental PK parameters after PO ($t_{1/2}$, T_{max}, C_{max}, AUC_{last}, AUC_{Inf}, AUC/D, AUC_{extr}, MRT, V_z, and Cl) and IV ($t_{1/2}$, C_0, AUC_{last}, AUC_{Inf}, AUC/D,

AUC$_{extr}$, MRT, V$_{ss}$, and Cl) administrations were obtained from the noncompartmental analysis of the plasma data using WinNonlin (best-fit mode). The mean values of the data at each time point were used in the parameter analysis.

References

1. Zhou, P.; Yang, X. L.; Wang, X. G.; Hu, B.; Zhang, L.; Zhang, W.; Si, H. R.; Zhu, Y.; Li, B.; Huang, C. L.; Chen, H. D.; Chen, J.; Luo, Y.; Guo, H.; Jiang, R. D.; Liu, M. Q.; Chen, Y.; Shen, X. R.; Wang, X.; Zheng, X. S.; Zhao, K.; Chen, Q. J.; Deng, F.; Liu, L. L.; Yan, B.; Zhan, F. X.; Wang, Y. Y.; Xiao, G. F.; Shi, Z. L., A pneumonia outbreak associated with a new coronavirus of probable bat origin. Nature 2020, *579* (7798), 270–273. doi:10.1038/s41586-020-2012-7.

2. Zhu, N.; Zhang, D.; Wang, W.; Li, X.; Yang, B.; Song, J.; Zhao, X.; Huang, B.; Shi, W.; Lu, R.; Niu, P.; Zhan, F.; Ma, X.; Wang, D.; Xu, W.; Wu, G.; Gao, G. F.; Tan, W.; China Novel Coronavirus, I.; Research, T., A Novel Coronavirus from Patients with Pneumonia in China, 2019. *N Engl J Med* 2020, *382* (8), 727–733. doi:10.1056/NEJMoa2001017.

3. Sheahan, T. P.; Sims, A. C.; Zhou, S.; Graham, R. L.; Pruijssers, A. J.; Agostini, M. L.; Leist, S. R.; Schafer, A.; Dinnon, K. H., 3rd; Stevens, L. J.; Chappell, J. D.; Lu, X.; Hughes, T. M.; George, A. S.; Hill, C. S.; Montgomery, S. A.; Brown, A. J.; Bluemling, G. R.; Natchus, M. G.; Saindane, M.; Kolykhalov, A. A.; Painter, G.; Harcourt, J.; Tamin, A.; Thornburg, N. J.; Swanstrom, R.; Denison, M. R.; Baric, R. S., An orally bioavailable broad-spectrum antiviral inhibits SARS-CoV-2 in human airway epithelial cell cultures and multiple coronaviruses in mice. Sci Transl Med 2020, *12* (541). doi:10.1126/scitranslmed.abb5883.

4. Owen, D. R.; Allerton, C. M. N.; Anderson, A. S.; Aschenbrenner, L.; Avery, M.; Berritt, S.; Boras, B.; Cardin, R. D.; Carlo, A.; Coffman, K. J.; Dantonio, A.; Di, L.; Eng, H.; Ferre, R.; Gajiwala, K. S.; Gibson, S. A.; Greasley, S. E.; Hurst, B. L.; Kadar, E. P.; Kalgutkar, A. S.; Lee, J. C.; Lee, J.; Liu, W.; Mason, S. W.; Noell, S.; Novak, J. J.; Obach, R. S.; Ogilvie, K.; Patel, N. C.; Pettersson, M.; Rai, D. K.; Reese, M. R.; Sammons, M. F.; Sathish, J. G.; Singh, R. S. P.; Steppan, C. M.; Stewart, A. E.; Tuttle, J. B.; Updyke, L.; Verhoest, P. R.; Wei, L.; Yang, Q.; Zhu, Y., An oral SARS-CoV-2 M(pro) inhibitor clinical candidate for the treatment of COVID-19. Science 2021, *374* (6575), 1586–1593. doi:10.1126/science.abl4784.

5. Lei, J.; Kusov, Y.; Hilgenfeld, R., Nsp3 of coronaviruses: Structures and functions of a large multi-domain protein. Antiviral Res 2018, *149*, 58–74. doi:10.1016/j.antiviral.2017.11.001.

6. Barretto, N.; Jukneliene, D.; Ratia, K.; Chen, Z.; Mesecar, A. D.; Baker, S. C., The papain-like protease of severe acute respiratory syndrome coronavirus has deubiquitinating activity. J Virol 2005, *79* (24), 15189–98. doi:10.1128/JVI.79.24.15189-15198.2005.

7. Lindner, H. A.; Fotouhi-Ardakani, N.; Lytvyn, V.; Lachance, P.; Sulea, T.; Menard, R., The papain-like protease from the severe acute respiratory syndrome coronavirus is a deubiquitinating enzyme. J Virol 2005, *79* (24), 15199–208. doi:10.1128/JVI.79.24.15199-15208.2005.

8. Lindner, H. A.; Lytvyn, V.; Qi, H.; Lachance, P.; Ziomek, E.; Menard, R., Selectivity in ISG15 and ubiquitin recognition by the SARS coronavirus papain-like protease. Arch Biochem Biophys **2007**, *466* (1), 8–

14. doi:10.1016/j.abb.2007.07.006.

9. Freitas, B. T.; Durie, I. A.; Murray, J.; Longo, J. E.; Miller, H. C.; Crich, D.; Hogan, R. J.; Tripp, R. A.; Pegan, S. D., Characterization and Noncovalent Inhibition of the Deubiquitinase and deISGylase Activity of SARS-CoV-2 Papain-Like Protease. ACS Infect Dis 2020, *6* (8), 2099–2109. doi:10.1021/acsinfecdis.0c00168.

10. Shin, D.; Mukherjee, R.; Grewe, D.; Bojkova, D.; Baek, K.; Bhattacharya, A.; Schulz, L.; Widera, M.; Mehdipour, A. R.; Tascher, G.; Geurink, P. P.; Wilhelm, A.; van der Heden van Noort, G. J.; Ovaa, H.; Muller, S.; Knobeloch, K. P.; Rajalingam, K.; Schulman, B. A.; Cinatl, J.; Hummer, G.; Ciesek, S.; Dikic, I., Papain-like protease regulates SARS-CoV-2 viral spread and innate immunity. Nature 2020. doi:10.1038/s41586-020-2601-5.

11. Rut, W.; Lv, Z.; Zmudzinski, M.; Patchett, S.; Nayak, D.; Snipas, S. J.; El Oualid, F.; Huang, T. T.; Bekes, M.; Drag, M.; Olsen, S. K., Activity profiling and crystal structures of inhibitor-bound SARS-CoV-2 papain-like protease: A framework for anti–COVID-19 drug design. Science Advances 2020, *6* (42). doi:10.1126/sciadv.abd4596.

12. Klemm, T.; Ebert, G.; Calleja, D. J.; Allison, C. C.; Richardson, L. W.; Bernardini, J. P.; Lu, B. G.; Kuchel, N. W.; Grohmann, C.; Shibata, Y.; Gan, Z. Y.; Cooney, J. P.; Doerflinger, M.; Au, A. E.; Blackmore, T. R.; van der Heden van Noort, G. J.; Geurink, P. P.; Ovaa, H.; Newman, J.; Riboldi-Tunnicliffe, A.; Czabotar, P. E.; Mitchell, J. P.; Feltham, R.; Lechtenberg, B. C.; Lowes, K. N.; Dewson, G.; Pellegrini, M.; Lessene, G.; Komander, D., Mechanism and inhibition of the papain-like protease, PLpro, of SARS-CoV-2. EMBO J 2020, e106275. doi:10.15252/embj.2020106275.

13. Ratia, K.; Saikatendu, K. S.; Santarsiero, B. D.; Barretto, N.; Baker, S. C.; Stevens, R. C.; Mesecar, A. D., Severe acute respiratory syndrome coronavirus papain-like protease: structure of a viral deubiquitinating enzyme. Proc Natl Acad Sci U S A 2006, *103* (15), 5717–22. doi:10.1073/pnas.0510851103.

14. Osipiuk, J.; Azizi, S. A.; Dvorkin, S.; Endres, M.; Jedrzejczak, R.; Jones, K. A.; Kang, S.; Kathayat, R. S.; Kim, Y.; Lisnyak, V. G.; Maki, S. L.; Nicolaescu, V.; Taylor, C. A.; Tesar, C.; Zhang, Y. A.; Zhou, Z.; Randall, G.; Michalska, K.; Snyder, S. A.; Dickinson, B. C.; Joachimiak, A., Structure of papain-like protease from SARS-CoV-2 and its complexes with non-covalent inhibitors. Nat Commun 2021, *12* (1), 743. doi:10.1038/s41467-021-21060-3.

15. Ratia, K.; Pegan, S.; Takayama, J.; Sleeman, K.; Coughlin, M.; Baliji, S.; Chaudhuri, R.; Fu, W.; Prabhakar, B. S.; Johnson, M. E.; Baker, S. C.; Ghosh, A. K.; Mesecar, A. D., A noncovalent class of papain-like protease/deubiquitinase inhibitors blocks SARS virus replication. Proc Natl Acad Sci U S A 2008, *105* (42), 16119–24. doi:10.1073/pnas.0805240105.

16. Ghosh, A. K.; Takayama, J.; Rao, K. V.; Ratia, K.; Chaudhuri, R.; Mulhearn, D. C.; Lee, H.; Nichols, D. B.; Baliji, S.; Baker, S. C.; Johnson, M. E.; Mesecar, A. D., Severe acute respiratory syndrome coronavirus papain-like novel protease inhibitors: design, synthesis, protein-ligand X-ray structure and biological evaluation. J Med Chem 2010, *53* (13), 4968–79. doi:10.1021/jm1004489.

17. Baez-Santos, Y. M.; Barraza, S. J.; Wilson, M. W.; Agius, M. P.; Mielech, A. M.; Davis, N. M.; Baker, S. C.; Larsen, S. D.; Mesecar, A. D., X-ray structural and biological evaluation of a series of potent and highly selective inhibitors of human coronavirus papain-like proteases. J Med Chem 2014, 57 (6), 2393–412. doi:10.1021/jm401712t.

18. Gao, X.; Qin, B.; Chen, P.; Zhu, K.; Hou, P.; Wojdyla, J. A.; Wang, M.; Cui, S., Crystal structure of SARS-CoV-2 papain-like protease. Acta Pharm Sin B 2021, 11 (1), 237–245. doi:10.1016/j.apsb.2020.08.014.

19. Baez-Santos, Y. M.; St John, S. E.; Mesecar, A. D., The SARS-coronavirus papain-like protease: structure, function and inhibition by designed antiviral compounds. Antiviral Res 2015, 115, 21–38. doi:10.1016/j.antiviral.2014.12.015.

20. Zaro, B. W.; Whitby, L. R.; Lum, K. M.; Cravatt, B. F., Metabolically Labile Fumarate Esters Impart Kinetic Selectivity to Irreversible Inhibitors. J Am Chem Soc 2016, 138 (49), 15841–15844. doi:10.1021/jacs.6b10589.

21. Resnick, E.; Bradley, A.; Gan, J.; Douangamath, A.; Krojer, T.; Sethi, R.; Geurink, P. P.; Aimon, A.; Amitai, G.; Bellini, D.; Bennett, J.; Fairhead, M.; Fedorov, O.; Gabizon, R.; Gan, J.; Guo, J.; Plotnikov, A.; Reznik, N.; Ruda, G. F.; Diaz-Saez, L.; Straub, V. M.; Szommer, T.; Velupillai, S.; Zaidman, D.; Zhang, Y.; Coker, A. R.; Dowson, C. G.; Barr, H. M.; Wang, C.; Huber, K. V. M.; Brennan, P. E.; Ovaa, H.; von Delft, F.; London, N., Rapid Covalent-Probe Discovery by Electrophile-Fragment Screening. J Am Chem Soc 2019, 141 (22), 8951–8968. doi:10.1021/jacs.9b02822.

22. Stein, R. L.; Chen, Z.; Melandri, F., Kinetic studies of isopeptidase T: modulation of peptidase activity by ubiquitin. Biochemistry 1995, 34 (39), 12616–23. doi:10.1021/bi00039a017.

23. Lee, H.; Lei, H.; Santarsiero, B. D.; Gatuz, J. L.; Cao, S.; Rice, A. J.; Patel, K.; Szypulinski, M. Z.; Ojeda, I.; Ghosh, A. K.; Johnson, M. E., Inhibitor recognition specificity of MERS-CoV papain-like protease may differ from that of SARS-CoV. ACS Chem Biol 2015, 10 (6), 1456–65. doi:10.1021/cb500917m.

24. Strelow, J. M., A Perspective on the Kinetics of Covalent and Irreversible Inhibition. SLAS Discov 2017, 22 (1), 3–20. doi:10.1177/1087057116671509.

25. Severson, W. E.; Shindo, N.; Sosa, M.; Fletcher, T., 3rd; White, E. L.; Ananthan, S.; Jonsson, C. B., Development and validation of a high-throughput screen for inhibitors of SARS CoV and its application in screening of a 100,000-compound library. J Biomol Screen 2007, 12 (1), 33–40. doi:10.1177/1087057106296688.

26. Swaim, C. D.; Canadeo, L. A.; Monte, K. J.; Khanna, S.; Lenschow, D. J.; Huibregtse, J. M., Modulation of Extracellular ISG15 Signaling by Pathogens and Viral Effector Proteins. Cell Rep 2020, 31 (11), 107772. doi:10.1016/j.celrep.2020.107772.

27. Armstrong, L. A.; Lange, S. M.; Dee Cesare, V.; Matthews, S. P.; Nirujogi, R. S.; Cole, I.; Hope, A.; Cunningham, F.; Toth, R.; Mukherjee, R.; Bojkova, D.; Gruber, F.; Gray, D.; Wyatt, P. G.; Cinatl, J.; Dikic, I.; Davies, P.; Kulathu, Y., Biochemical characterization of protease activity of Nsp3 from SARS-CoV-2 and its inhibition by nanobodies. PLoS One 2021, 16 (7), e0253364. doi:10.1371/journal.pone.0253364.

28. Kalgutkar, A. S.; Frederick, K. S.; Chupka, J.; Feng, B.; Kempshall, S.; Mireles, R. J.; Fenner, K. S.; Troutman, M. D., N-(3,4-dimethoxyphenethyl)-4-(6,7-dimethoxy-3,4-dihydroisoquinolin-2[1H]-yl)-6,7-dimethoxyquinazolin-2-amine (CP-100,356) as a "chemical knock-out equivalent" to assess the impact of efflux transporters on oral drug absorption in the rat. J Pharm Sci 2009, *98* (12), 4914–27. doi:10.1002/jps.21756.

29. Boudreaux, D. A.; Maiti, T. K.; Davies, C. W.; Das, C., Ubiquitin vinyl methyl ester binding orients the misaligned active site of the ubiquitin hydrolase UCHL1 into productive conformation. Proc Natl Acad Sci U S A 2010, *107* (20), 9117–22. doi:10.1073/pnas.0910870107.

30. Bishop, P.; Rocca, D.; Henley, J. M., Ubiquitin C-terminal hydrolase L1 (UCH-L1): structure, distribution and roles in brain function and dysfunction. Biochem J 2016, *473* (16), 2453–62. doi:10.1042/BCJ20160082.

31. Clerici, M.; Luna-Vargas, M. P.; Faesen, A. C.; Sixma, T. K., The DUSP-Ubl domain of USP4 enhances its catalytic efficiency by promoting ubiquitin exchange. Nat Commun 2014, *5*, 5399. doi:10.1038/ncomms6399.

32. Cruciani, G.; Carosati, E.; De Boeck, B.; Ethirajulu, K.; Mackie, C.; Howe, T.; Vianello, R., MetaSite: understanding metabolism in human cytochromes from the perspective of the chemist. J Med Chem 2005, *48* (22), 6970–9. doi:10.1021/jm050529c.

33. Burgey, C. S.; Robinson, K. A.; Lyle, T. A.; Sanderson, P. E.; Lewis, S. D.; Lucas, B. J.; Krueger, J. A.; Singh, R.; Miller-Stein, C.; White, R. B.; Wong, B.; Lyle, E. A.; Williams, P. D.; Coburn, C. A.; Dorsey, B. D.; Barrow, J. C.; Stranieri, M. T.; Holahan, M. A.; Sitko, G. R.; Cook, J. J.; McMasters, D. R.; McDonough, C. M.; Sanders, W. M.; Wallace, A. A.; Clayton, F. C.; Bohn, D.; Leonard, Y. M.; Detwiler, T. J., Jr.; Lynch, J. J., Jr.; Yan, Y.; Chen, Z.; Kuo, L.; Gardell, S. J.; Shafer, J. A.; Vacca, J. P., Metabolism-directed optimization of 3-aminopyrazinone acetamide thrombin inhibitors. Development of an orally bioavailable series containing P1 and P3 pyridines. J Med Chem 2003, *46* (4), 461–73. doi:10.1021/jm020311f.

34. Gant, T. G., Using deuterium in drug discovery: leaving the label in the drug. J Med Chem 2014, *57* (9), 3595–611. doi:10.1021/jm4007998.

35. Trunzer, M.; Faller, B.; Zimmerlin, A., Metabolic soft spot identification and compound optimization in early discovery phases using MetaSite and LC-MS/MS validation. J Med Chem **2009**, *52* (2), 329–35. doi:10.1021/jm8008663.

36. Smith, P. W.; Wyman, P. A.; Lovell, P.; Goodacre, C.; Serafinowska, H. T.; Vong, A.; Harrington, F.; Flynn, S.; Bradley, D. M.; Porter, R.; Coggon, S.; Murkitt, G.; Searle, K.; Thomas, D. R.; Watson, J. M.; Martin, W.; Wu, Z.; Dawson, L. A., New quinoline NK3 receptor antagonists with CNS activity. Bioorg Med Chem Lett **2009**, *19* (3), 837–40. doi:10.1016/j.bmcl.2008.12.005.

37. Shen, Z.; Ratia, K.; Cooper, L.; Kong, D.; Lee, H.; Kwon, Y.; Li, Y.; Alqarni, S.; Huang, F.; Dubrovskyi, O.; Rong, L.; Thatcher, G. R. J.; Xiong, R., Design of SARS-CoV-2 PLpro Inhibitors for COVID-19 Antiviral Therapy Leveraging Binding Cooperativity. J Med Chem **2022**, *65* (4), 2940–2955. doi:10.1021/acs.jmedchem.1c01307.

38. Calleja, D. J.; Lessene, G.; Komander, D., Inhibitors of SARS-CoV-2 PLpro. Front Chem 2022, *10*, 876212. doi:10.3389/fchem.2022.876212.

39. Tan, H.; Hu, Y.; Jadhav, P.; Tan, B.; Wang, J., Progress and Challenges in Targeting the SARS-CoV-2 Papain-like Protease. J Med Chem **2022**, *65* (11), 7561−7580. doi:10.1021/acs.jmedchem.2c00303.

40. Liebschner, D.; Afonine, P. V.; Baker, M. L.; Bunkoczi, G.; Chen, V. B.; Croll, T. I.; Hintze, B.; Hung, L. W.; Jain, S.; McCoy, A. J.; Moriarty, N. W.; Oeffner, R. D.; Poon, B. K.; Prisant, M. G.; Read, R. J.; Richardson, J. S.; Richardson, D. C.; Sammito, M. D.; Sobolev, O. V.; Stockwell, D. H.; Terwilliger, T. C.; Urzhumtsev, A. G.; Videau, L. L.; Williams, C. J.; Adams, P. D., Macromolecular structure determination using X-rays, neutrons and electrons: recent developments in Phenix. Acta Crystallogr D Struct Biol 2019, *75* (Pt 10), 861−877. doi:10.1107/S2059798319011471.

41. Burnley, B. T.; Afonine, P. V.; Adams, P. D.; Gros, P., Modelling dynamics in protein crystal structures by ensemble refinement. Elife 2012, *1*, e00311. doi:10.7554/eLife.00311.

42. Case, D. A.; Belfon, K.; Ben-Shalom, I. Y.; Brozell, S. R.; Cerutti, D. S.; Cheatham III, T. E.; Cruzeiro, V. W. D.; Darden, T. A.; Duke, R. E.; Giambasu, G.; Gilson, M. K.; Gohlke, H.; Goetz, A. W.; Harris, R.; Izadi, S.; Izmailov, S. A.; Kasavajhala, K.; Kovalenko, A.; Krasny, R.; Kurtzman, T.; Lee, T. S.; LeGrand, S.; Li, P.; Lin, C.; Liu, J.; Luchko, T.; Luo, R.; Man, V.; Merz, K. M.; Miao, Y.; Mikhailovskii, O.; Monard, G.; Nguyen, H.; Onufriev, A.; Pan, F.; Pantano, S.; Qi, R.; Roe, D. R.; Roitberg, A.; Sagui, C.; Schott-Verdugo, S.; Shen, J.; Simmerling, C.; Skrynnikov, N. R.; Smith, J.; Swails, J.; Walker, R. C.; Wang, J.; Wilson, L.; Wolf, R. M.; Wu, X.; Xiong, Y.; Xue, Y.; York, D. M.; Kollman, P. A., AMBER 2020. University of California, San Francisco, 2020.

43. Maier, J. A.; Martinez, C.; Kasavajhala, K.; Wickstrom, L.; Hauser, K. E.; Simmerling, C., ff14SB: Improving the Accuracy of Protein Side Chain and Backbone Parameters from ff99SB. J Chem Theory Comput **2015**, *11* (8), 3696−713. doi:10.1021/acs.jctc.5b00255.

44. Jorgensen, W. L.; Chandrasekhar, J.; Madura, J. D.; Impey, R. W.; Klein, M. L., Comparison of simple potential functions for simulating liquid water. The Journal of Chemical Physics **1983**, *79* (2), 926−935. doi:10.1063/1.445869.

45. Ravindranath, P. A.; Forli, S.; Goodsell, D. S.; Olson, A. J.; Sanner, M. F., AutoDockFR: Advances in Protein-Ligand Docking with Explicitly Specified Binding Site Flexibility. PLoS Comput Biol 2015, *11* (12), e1004586. doi:10.1371/journal.pcbi.1004586.

46. O'Boyle, N. M.; Banck, M.; James, C. A.; Morley, C.; Vandermeersch, T.; Hutchison, G. R., Open Babel: An open chemical toolbox. J Cheminform 2011, *3*, 33. doi:10.1186/1758-2946-3-33.

47. Landrum, G., RDKit: Open-source cheminformatics. 2006.

48. Morris, G. M.; Huey, R.; Lindstrom, W.; Sanner, M. F.; Belew, R. K.; Goodsell, D. S.; Olson, A. J., AutoDock4 and AutoDockTools4: Automated docking with selective receptor flexibility. J Comput Chem 2009, *30* (16), 2785−91. doi:10.1002/jcc.21256.

49. Schrödinger, L., The PyMOL Molecular Graphics System, Version 2.4. 2021.

50. Fulmer, G. R.; Miller, A. J. M.; Sherden, N. H.; Gottlieb, H. E.; Nudelman, A.; Stoltz, B. M.; Bercaw, J. E.; Goldberg, K. I., NMR Chemical Shifts of Trace Impurities: Common Laboratory Solvents, Organics,

and Gases in Deuterated Solvents Relevant to the Organometallic Chemist. Organometallics 2010, *29* (9), 2176–2179. doi:10.1021/om100106e.

51. Leite, W. C.; Weiss, K. L.; Phillips, G.; Zhang, Q.; Qian, S.; Tsutakawa, S. E.; Coates, L.; O'Neill, H., Conformational Dynamics in the Interaction of SARS-CoV-2 Papain-like Protease with Human Interferon-Stimulated Gene 15 Protein. J Phys Chem Lett **2021**, *12* (23), 5608–5615. doi:10.1021/acs.jpclett.1c00831.

52. Donnelly, D. P.; Rawlins, C. M.; DeHart, C. J.; Fornelli, L.; Schachner, L. F.; Lin, Z.; Lippens, J. L.; Aluri, K. C.; Sarin, R.; Chen, B.; Lantz, C.; Jung, W.; Johnson, K. R.; Koller, A.; Wolff, J. J.; Campuzano, I. D. G.; Auclair, J. R.; Ivanov, A. R.; Whitelegge, J. P.; Pasa-Tolic, L.; Chamot-Rooke, J.; Danis, P. O.; Smith, L. M.; Tsybin, Y. O.; Loo, J. A.; Ge, Y.; Kelleher, N. L.; Agar, J. N., Best practices and benchmarks for intact protein analysis for top-down mass spectrometry. Nat Methods 2019, *16* (7), 587–594. doi:10.1038/s41592-019-0457-0.

53. Strohalm, M.; Kavan, D.; Novak, P.; Volny, M.; Havlicek, V., mMass 3: a cross-platform software environment for precise analysis of mass spectrometric data. Anal Chem **2010**, *82* (11), 4648–51. doi:10.1021/ac100818g.

54. Nicholson, B.; Leach, C. A.; Goldenberg, S. J.; Francis, D. M.; Kodrasov, M. P.; Tian, X.; Shanks, J.; Sterner, D. E.; Bernal, A.; Mattern, M. R.; Wilkinson, K. D.; Butt, T. R., Characterization of ubiquitin and ubiquitin-like-protein isopeptidase activities. Protein Sci 2008, *17* (6), 1035–43. doi:10.1110/ps.083450408.

55. Kabsch, W., Xds. Acta Crystallogr D Biol Crystallogr 2010, *66* (Pt 2), 125–32. doi:10.1107/S0907444909047337.

56. Navaza, J., AMoRe: an automated package for molecular replacement. Acta Crystallographica Section A Foundations of Crystallography 1994, *50* (2), 157–163. doi:10.1107/s0108767393007597.

57. Emsley, P.; Lohkamp, B.; Scott, W. G.; Cowtan, K., Features and development of Coot. Acta Crystallogr D Biol Crystallogr 2010, *66* (Pt 4), 486–501. doi:10.1107/S0907444910007493.

58. Murshudov, G. N.; Vagin, A. A.; Dodson, E. J., Refinement of macromolecular structures by the maximum-likelihood method. Acta Crystallogr D Biol Crystallogr 1997, *53* (Pt 3), 240–55. doi:10.1107/S0907444996012255.

59. Bocci, G.; Bradfute, S. B.; Ye, C.; Garcia, M. J.; Parvathareddy, J.; Reichard, W.; Surendranathan, S.; Bansal, S.; Bologa, C. G.; Perkins, D. J.; Jonsson, C. B.; Sklar, L. A.; Oprea, T. I., Virtual and In Vitro Antiviral Screening Revive Therapeutic Drugs for COVID-19. ACS Pharmacol Transl Sci 2020, *3* (6), 1278–1292. doi:10.1021/acsptsci.0c00131.

60. Harcourt, J.; Tamin, A.; Lu, X.; Kamili, S.; Sakthivel, S. K.; Murray, J.; Queen, K.; Tao, Y.; Paden, C. R.; Zhang, J.; Li, Y.; Uehara, A.; Wang, H.; Goldsmith, C.; Bullock, H. A.; Wang, L.; Whitaker, B.; Lynch, B.; Gautam, R.; Schindewolf, C.; Lokugamage, K. G.; Scharton, D.; Plante, J. A.; Mirchandani, D.; Widen, S. G.; Narayanan, K.; Makino, S.; Ksiazek, T. G.; Plante, K. S.; Weaver, S. C.; Lindstrom, S.; Tong, S.; Menachery, V. D.; Thornburg, N. J., Severe Acute Respiratory Syndrome Coronavirus 2 from Patient

with Coronavirus Disease, United States. Emerg Infect Dis 2020, *26* (6), 1266–1273. doi:10.3201/eid2606.200516.

61. Liu, H.; Iketani, S.; Zask, A.; Khanizeman, N.; Bednarova, E.; Forouhar, F.; Fowler, B.; Hong, S. J.; Mohri, H.; Nair, M. S.; Huang, Y.; Tay, N. E. S.; Lee, S.; Karan, C.; Resnick, S. J.; Quinn, C.; Li, W.; Shion, H.; Xia, X.; Daniels, J. D.; Bartolo-Cruz, M.; Farina, M.; Rajbhandari, P.; Jurtschenko, C.; Lauber, M. A.; McDonald, T.; Stokes, M. E.; Hurst, B. L.; Rovis, T.; Chavez, A.; Ho, D. D.; Stockwell, B. R., Development of optimized drug-like small molecule inhibitors of the SARS-CoV-2 3CL protease for treatment of COVID-19. Nat Commun 2022, *13* (1), 1891. doi:10.1038/s41467-022-29413-2.

62. Obach, R. S. B., J.G.; Liston, T.E.; Silber, B.M.; Jones, B.C.; MacIntyre, F.; Rance, D.J.; Wastall, P, The prediction of hyman pharmacokinetic parameters from preclinical and in vitro metabolism data. J Pharmacol Exp Ther 1997, *283*, 46–58.
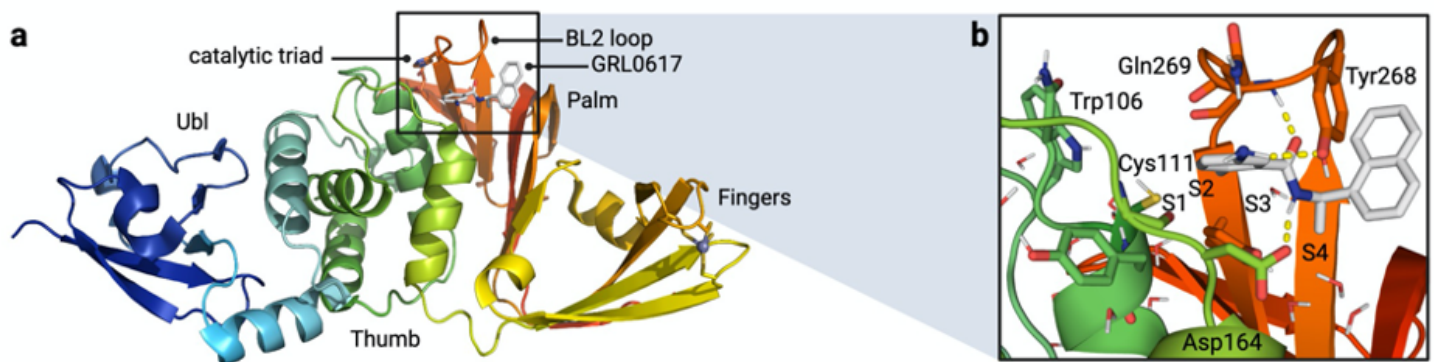
Figures

Figure 1

(a) Structure and domains of PLpro from SARS-CoV-2 (PDB entry 7JIR[14]). Selected features are labeled.
(b) Interactions between PLpro and the noncovalent inhibitor GRL0617.
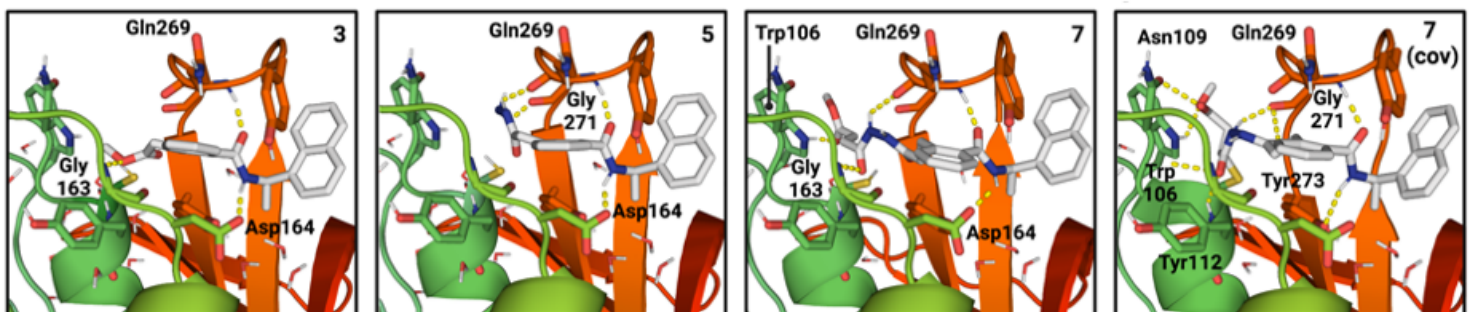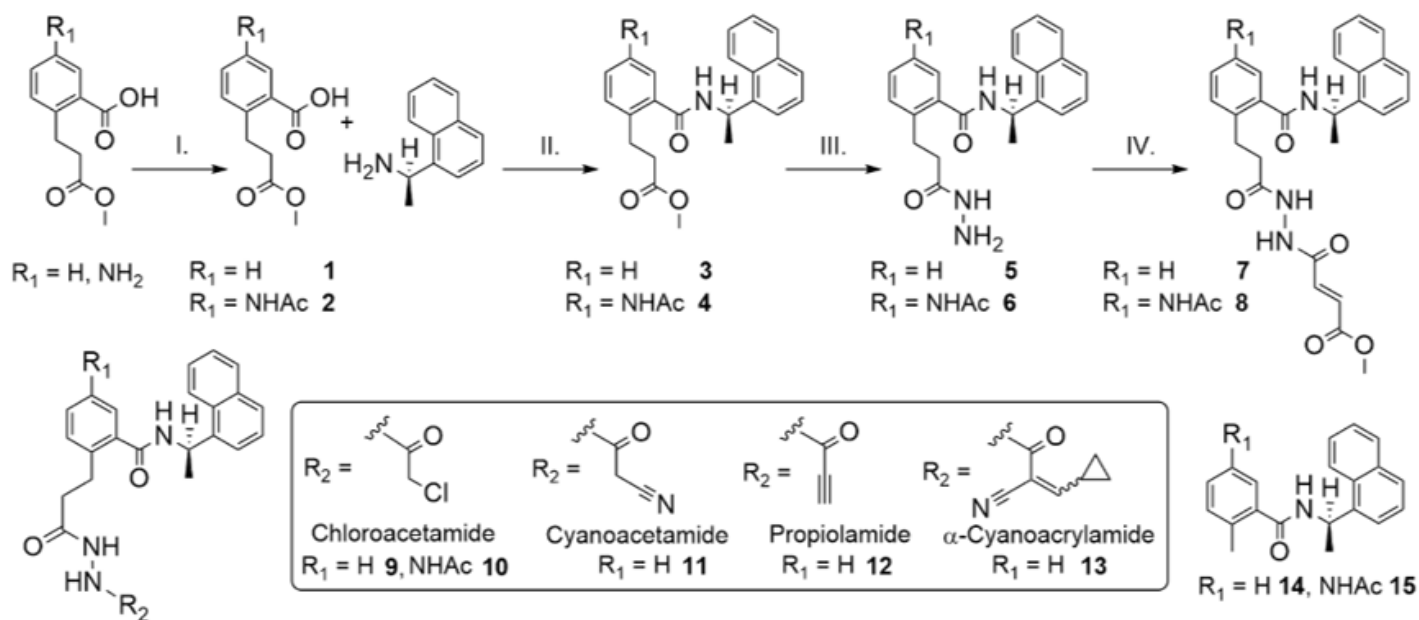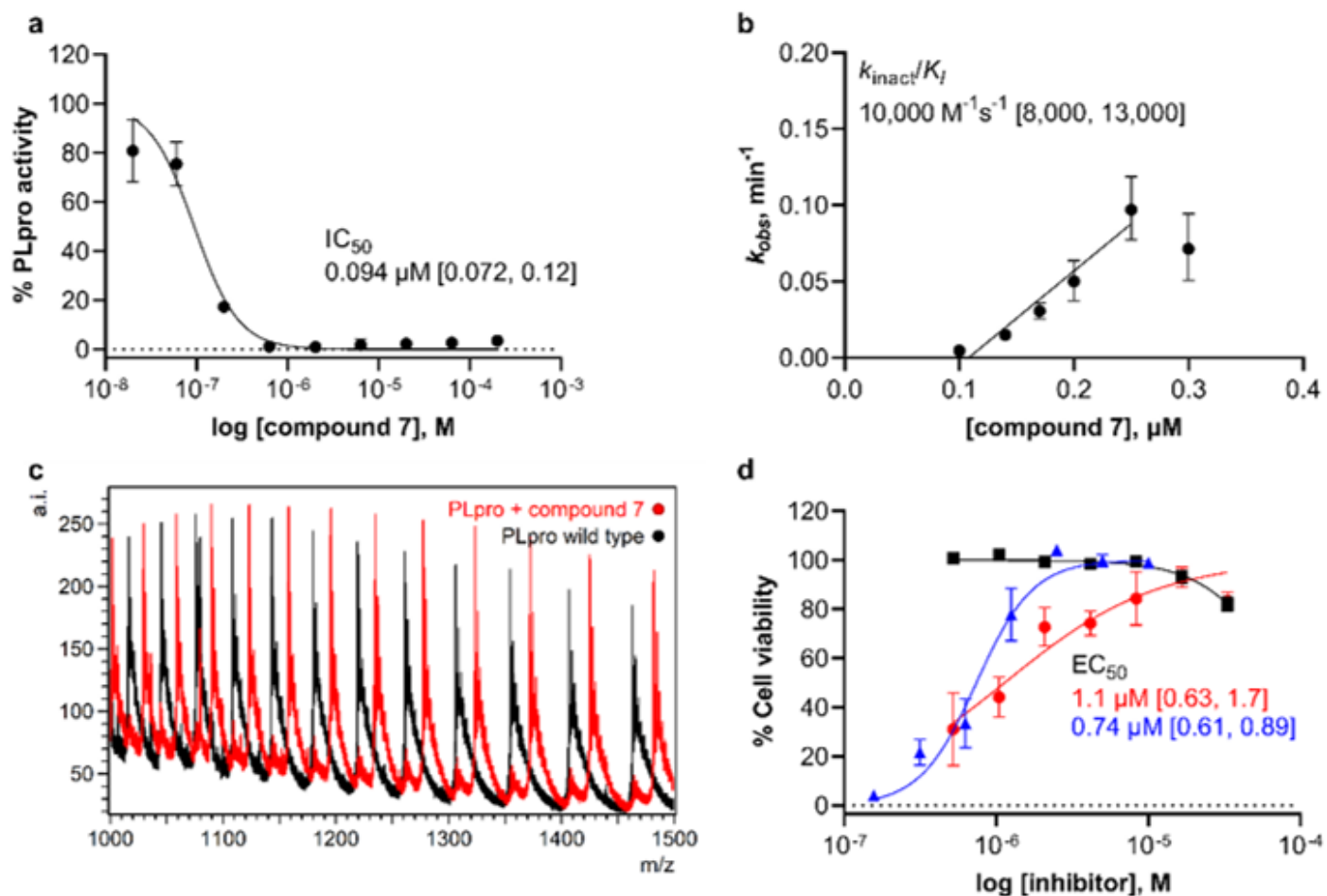

Figure 2

Left to right: Docked poses of compound **3**, compound **5**, and compound **7** docked both noncovalently and covalently. Structures of compounds are shown in **Figure 3**. Polar hydrogens have been added. Docked poses for additional inhibitor candidates are shown in **Figure S2**. Ligand carbons are shown in gray and predicted protein-ligand interactions are shown as dashed yellow lines.
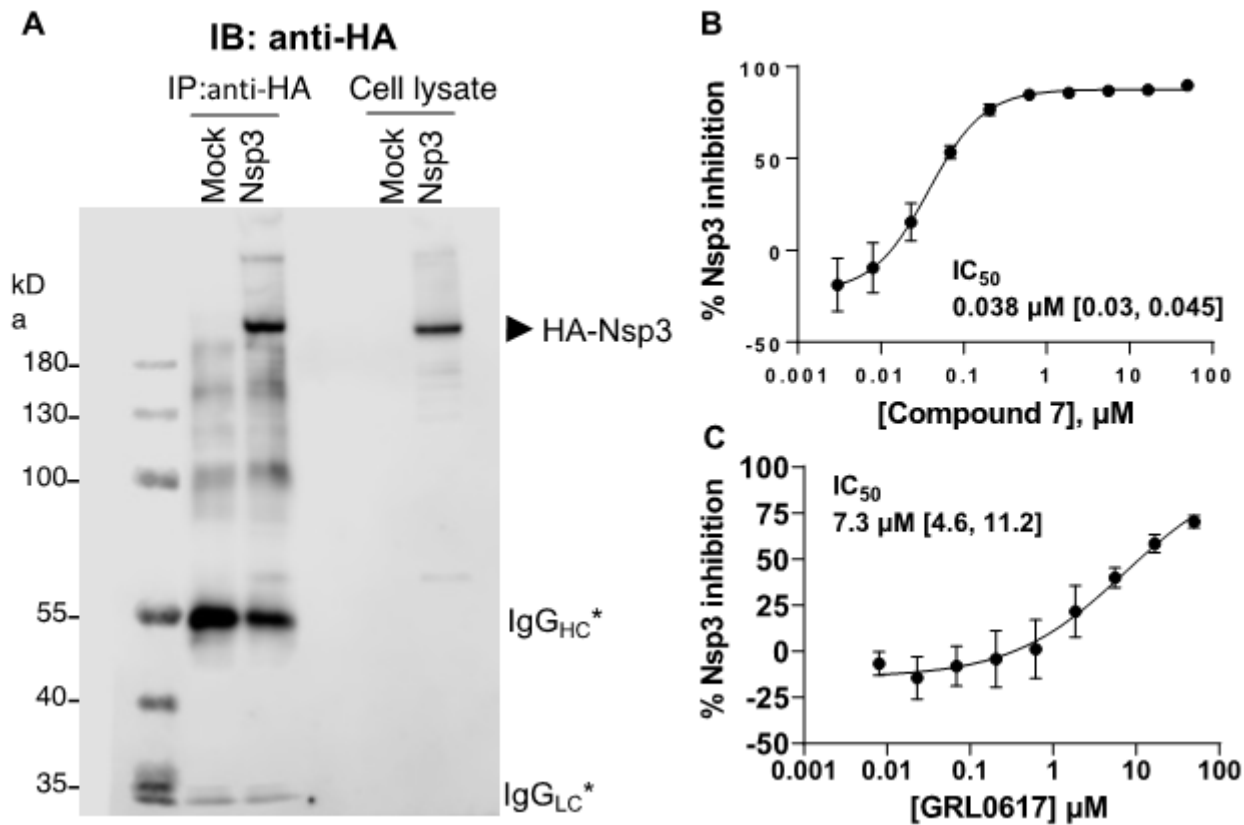

Figure 3

Synthesis of compounds **2-15**. Reaction conditions with yields in parentheses: **I**. Ac$_2$O, AcOH, DCM, 55%; **II**. HATU, DIPEA, DCM (**3**, 83%; **4**, 91%); **III**. N$_2$H$_4$·H$_2$O, EtOH (**5** and **6**, 97%); **IV**. methyl (*E*)-4-chloro-4-oxobut-2-enoate, DIPEA, DCM for **7** (56%), and K$_2$CO$_3$, DMF for **8** (34%). Compounds **9** (50%), **10** (37%), **11** (56%), **12** (23%), and **13** (60%) were prepared with the corresponding acid chlorides under conditions described for step IV. Compounds **14** (89%) and **15** (83%) were prepared analogously to step II with 2-methylbenzoic acid and 5-acetamido-2-methylbenzoic acid, respectively.
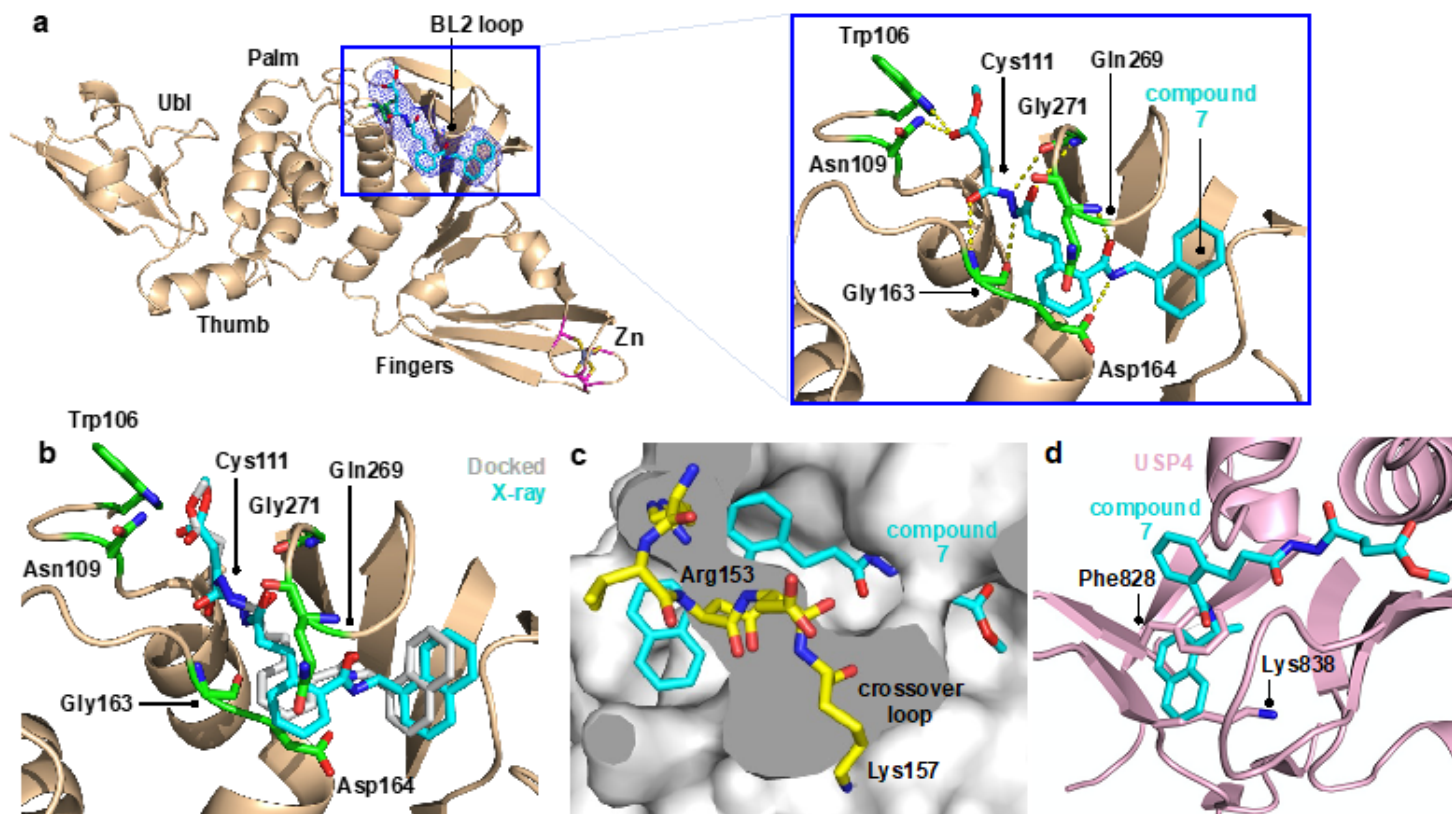
Figure 4

Characterization of a designed covalent PLpro inhibitor, compound 7. (**a**) Fluorogenic peptide activity assay after 30-min preincubation with compound **7**. Data points are the average of $n = 2$ independent samples ± range and are representative of $n = 3$ independent experiments. IC_{50} is the concentration at which 50% inhibition was observed, and bracketed values are the 95% confidence interval. Curve is the nonlinear regression to the normalized inhibitor dose response equation. (**b**) Time-dependent characterization with a fluorogenic peptide assay. Data points are k_{obs} values determined by fitting the exponential decay equation to initial rates determined at various inhibitor concentrations and preincubation times, normalized to no preincubation. k_{obs} values were determined from $n = 2$ independent experiments with $n = 2$ independent samples each ± 95% confidence interval of the nonlinear regression. Line represents the linear regression yielding as its slope the second-order rate constant (k_{inact}/K_I). (**c**) Intact protein ESI-MS spectra of PLpro (black) and PLpro incubated with **7** (red); a.i., arbitrary intensity; m/z, mass-to-charge ratio. (**d**) Percent viability of Vero E6 cells after 48 h following pretreatment with **7** (black squares), pretreatment with **7** and infection with SARS-CoV-2 (red circles), or pretreatment with remdesivir and infected with SARS-CoV-2 (blue triangles). Data points are the average of $n = 2$ independent samples ± range and are representative of $n = 2$ independent experiments. EC_{50} is the

concentration at which 50% effect was observed and bracketed values are the 95% confidence interval. Curves are nonlinear regressions to the normalized dose response equation.

Figure 5

Inhibition of the deISGylase activity of full-length SARS-CoV-2 hemagglutinin (HA)-Nsp3 transiently expressed in HEK293T cells. (**a**) Anti-HA beads after immunoprecipitation and whole cell lysates probed with anti-HA antibody. The asterisk indicates IgG heavy and light chains. Anti-HA beads were assayed for Nsp3 deISGylase activity using an ISG15-CHOP2 assay in the presence of the dose range of (**b**) compound **7** or (**c**) GRL0617.

Figure 6

Crystal structure of SARS-CoV-2 PLpro in complex with inhibitor 7. (**a**) Overall structure and interactions between the active site residues and **7** (cyan sticks). The electron density for **7** is shown in blue mesh (Fo - Fc omit map contoured at 1.5 σ). (**b**) Superposition of the covalently docked model of **7** (grey sticks) and the co-crystal structure of PLpro and **7** (cyan sticks). (**c**) Structural basis for selectivity toward PLpro. Superposition of **7** bound to PLpro onto human deubiquitinase UCHL1[29] (PDB entry 3KW5). The crossover loop of UCHL1, 153-RVDDK-157, covers the narrow groove and blocks the naphthylmethylamine core of **7** from binding. The crossover loop is longer and, in some cases, more disordered in UCHL3 and UCHL5 (see for example ref 30). (**d**) Superposition of **7** bound to PLpro onto human USP4[31] (PDB entry 2Y6E). Severe steric clashes are present between the naphthyl ring of **7** and Phe828 and Lys838 of USP4 (light pink sticks), both of which are conserved in 80% of human USPs.

Supplementary Files

This is a list of supplementary files associated with this preprint. Click to download.

- supplementarydatafile1docking.xlsx
- SupplementaryDataFile2.pdf
- D9100058695valreportfullP1.pdf

- plproSI.docx